International Journal of Heat and Mass Transfer 123 (2018) 911–927

Contents lists available at ScienceDirect

International Journal of Heat and Mass Transfer

journal homepage: www.elsevier.com/locate/ijhmt

A semi-analytical model for detailed 3D heat flow in shallow geothermal systems

Noori BniLam [a,b,*], Rafid Al-Khoury [a], Arsha Shiri [a], L.J. Sluys [a]

[a] Faculty of Civil Engineering and Geosciences, Computational Mechanics Chair, Delft University of Technology, P.O. Box 5048, 2600 GA Delft, The Netherlands
[b] University of Antwerp – imec, IDLab Research Group, Antwerp, Belgium

ARTICLE INFO

Article history:
Received 2 December 2017
Received in revised form 3 March 2018
Accepted 3 March 2018
Available online 20 March 2018

Keywords:
BHE
GHP
GSHP
Shallow geothermal system
Multiple borehole heat exchangers
Multilayer system
Spectral element method

ABSTRACT

A semi-analytical model for simulating transient conductive-convective heat flow in a three-dimensional shallow geothermal system consisting of multiple borehole heat exchangers (BHE) embedded in a multilayer soil mass is introduced. The model is formulated in three steps, starting from an axial symmetric system and ending in a 3D multilayer, multiple BHE system. In step 1, the model is formulated as a single BHE embedded in an axial symmetric homogeneous soil layer, and the governing heat equations are solved analytically using the fast Fourier transform, the eigenfunction expansion and the modified Bessel function. In step 2, the model is extended to incorporate multiple layers using the spectral element method. And in step 3, the model is extended to incorporate multiple borehole heat exchangers using a superposition technique suitable for Dirichlet boundary conditions. The ensuing computational model solves detailed three-dimensional heat flow using minimal CPU time and capacity. The number of the required spectral elements is equal to the number of soil layers embedded in which any number of borehole heat exchangers with any layout configuration. A verification example illustrating the model accuracy and numerical examples illustrating its computational capabilities are given. Despite the apparent rigor of the proposed model, its high accuracy and computational efficiency make it suitable for engineering practice.

1. Introduction

Extracting thermal energy from relatively shallow depths has become an established technology, and shallow geothermal systems known as geothermal heat pumps (GHP), ground source heat pumps (GSHP) or borehole heat exchangers (BHE) are in use all over the world. A BHE works by circulating a fluid, mostly water with antifreeze, through a closed loop of polyethylene pipe that is inserted in a borehole embedded in a soil mass. The borehole is filled with grout to fix the polyethylene pipe and to ensure a good thermal interaction with the soil. Several types of BHE are available in practice. In this work, the BHE is assumed to consist of a vertical single U-tube filled with circulating water and embedded in grout.

The borehole heat exchanger is a slender heat pipe with dimensions of the order of 30 mm in diameter for the U-tube, and 150 mm in diameter and 100 m in length for the borehole. The U-tube carries a circulating fluid that collects heat (or ejects heat) from (or to) the surrounding soil via convection-conduction heat transfer mechanisms.

In practice, shallow geothermal systems consist of multiple borehole heat exchangers embedded in a multilayer soil mass. Computational modelling of such a system, in spite of the bulk of existing models, is yet state of the art due to the combination of the extreme slenderness of the boreholes heat exchangers, the presence of multiple components with different thermal properties and the involved heat convection. Consequently, several theoretical and computational assumptions and approximations have been introduced in order to circumvent this computationally challenging combination and obtain feasible solutions. All known solution techniques, such as analytical, semi-analytical and numerical, have been utilized for this purpose. Nevertheless, in spite of the versatility of the numerical methods, analytical and semi-analytical solutions are yet preferable because of their comparatively little demands on computational power and ease of use in engineering practice. In Al-Khoury [2] a thorough review of models utilized in this field is given. In this paper, focus is placed on models based on the semi-analytical solution technique.

Eskilson and Claesson [9] introduced a semi-analytical model for heat flow in a borehole heat exchanger constituting two fluid channels and a borehole wall, embedded in an axial symmetric soil

* Corresponding author at: University of Antwerp – imec, IDLab Research Group, Antwerp, Belgium.
E-mail addresses: n.h.n.bnilam@tudelft.nl, Noori.Bnilam@uantwerpen.be (N. BniLam).

https://doi.org/10.1016/j.ijheatmasstransfer.2018.03.010
0017-9310/

mass. The governing heat equations of the two fluid channels are solved using the Laplace transform and that for the soil mass using the finite difference method. They extended the model to 3D by use of the principle of superposition to account for multiple heat sources. Their solution is effective for relatively long term analyses and for a symmetric heat sources configuration.

Pasquier and Marcotte [11] introduced a semi-analytical model for heat flow in a solid mass subjected to multiple infinite line heat sources with time-varying heat fluxes and temperatures. They applied the fast Fourier transform for the temporal domain and the superposition principle for the spatial domain. The thermal interaction between the involved heat sources is solved using an iterative algorithm.

Erol et al. [8] introduced a modified Green's function for heat flow in a porous domain subjected to a constant line heat source with a finite length. The convolution theory is utilized to solve the initial and boundary value problem for a single heat source. For multiple heat sources, they utilized the superposition principle by summing up the temporal convolved functions of the heat sources.

Raymond and Lamarche [12] analyzed the effect of multiple layers in determining the thermal parameters from the thermal response test (TRT) results. They adopted an analytical computer code (MLU), which was originally developed for transient water flow in layered aquifers, to describe conductive heat transfer in shallow geothermal systems constituting multiple layers and subjected to a variable heat injection rate. The Laplace transform is utilized to solve the system of partial differential equations describing heat flow in the layered system.

Abdelaziz et al. [1] extended the finite line heat source solution to a multiple segment finite line heat source resembling a layered soil profile. The temperature of the heterogeneous domain is obtained by summing up the temperature in a typical homogeneous domain with that obtained due to the presence of other layers. The latter is calculated by assuming a composite system constituting smeared thermal parameters, described as a function of the relative distances of the layers from the point of interest.

Apparently, semi-analytical solutions for heat flow in multiple heat sources embedded in a homogeneous soil mass exist. Also, semi-analytical solutions for a single heat source embedded in a multilayer system exist. However, semi-analytical solutions for multiple heat sources embedded in a multilayer soil mass do not exist. This constitutes the objective of this work.

In a previous work, BniLam and Al-Khoury [3] introduced an analytical model for transient heat flow in an infinite soil mass subjected to multiple cylindrical heat sources. In a later work, BniLam and Al-Khoury [4] introduced an axial-symmetric spectral element model for heat flow in a borehole heat exchanger embedded in a multilayer system. In this paper, these two models are elaborated and put together to formulate a detailed three-dimensional shallow geothermal system with any arbitrary layout configuration. The multiple infinite cylindrical heat sources of the first model are replaced by multiple finite borehole heat exchangers, and are incorporated in the multilayer system of the second model. This entails establishing a tailored thermal interaction between the borehole and the surrounding soil mass, and between the boreholes themselves. The superposition principle for Dirichlet boundary conditions, introduced in BniLam and Al-Khoury [3], is tailored to the multiple BHE case. By this, the soil temperature amplitudes at the borehole locations are coupled to the temperatures in the BHE components, followed by coupling all involved boreholes via a matrix technique. Additionally, in this paper, we modified the formulation of the 2-noded spectral element. In BniLam and Al-Khoury [4], the spectral element was formulated based on the first kind Bessel function J_0, which is suitable for a line source case where the borehole and the soil mass share and coincide on the axis of symmetry. In the current paper, the solution is modified to lead to the use of the modified Bessel function K_0, which is suitable for a cylindrical source case where the borehole and the soil mass share the axis of symmetry, but the soil mass starts at the radius of the borehole. The latter function is more physical in representing the cylindrical nature of the BHE-soil interaction, and it has no roots to be determined and summed over. Details of the modelling approach are given hereafter.

2. Modeling approach

A shallow geothermal system, particularly a geothermal heat pump, consists basically of two thermally interacting domains: the borehole heat exchanger and the soil mass. In practice, the system consists of several borehole heat exchangers embedded in a multilayer layer soil mass. Solving heat flow in such a three-dimensional, nonhomogeneous geometry typically requires the use of a numerical method, such as the finite element, the finite volume or the finite difference method. However, these methods, and due to the disproportionate geometry of the system and the presence of the convective heat transfer mechanism, might require significant CPU time and capacity. To avoid this, here, a semi-analytical solution is proposed. The heat flow in this system is modelled in three steps, starting from an axial symmetric system and ending in a 3D multilayer, multiple BHE system, as outlined hereafter.

Step 1: The model is first formulated as a single BHE embedded in a semi-infinite homogeneous soil mass. The borehole heat exchanger is modelled as 1D with its axis coinciding on the vertical z-axis. The 1D assumption is reasonably valid because of the extreme slenderness of the borehole that makes the temperature gradient in the radial direction of the BHE components negligible. A single U-tube consisting of pipe-in, pipe-out and grout is considered in this study, but extension to other BHE types is straightforward. The BHE components coincide geometrically on each other, but thermally interacting with each other.

The soil mass, on the other hand, is modelled as a semi-infinite, axial symmetric domain with its axis of symmetry coinciding with the centerline of the borehole heat exchanger (z-axis). In principle, the heat equation for this domain must be formulated in the r, z - coordinate system. Solving this equation analytically would require an extra separation of variables and the determination of an additional Fourier coefficient. To circumvent this, we introduced

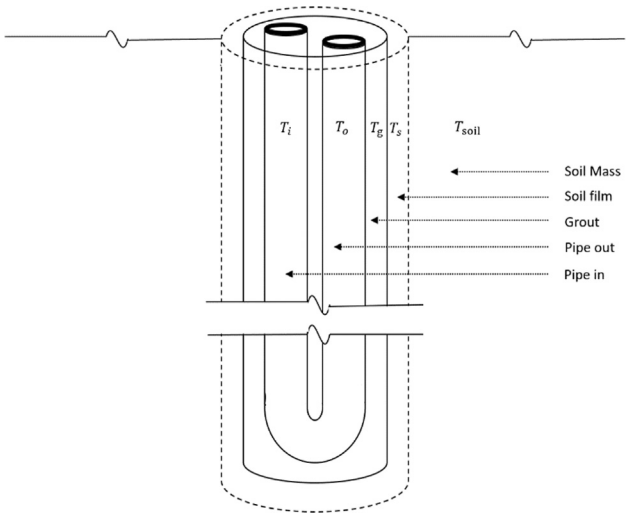

Fig. 1. A schematic representation of a single U-tube BHE and its surrounding soil mass.

a soil film connecting the BHE to the soil mass, as shown in Fig. 1. The soil film has the soil mass properties, and its heat equation describes the temperature distribution in the soil mass along the z direction, which acts as the amplitude to the radial direction (r -coordinate). By this, the soil mass heat equation can be formulated in the radial direction only, making it relatively easy to solve. However, adding a soil film entails assigning a thickness, which is apparently hypothetical (see Fig. 2). As the soil film temperature acts as the amplitude to the soil mass temperature, the choice of its thickness can affect the temperature distributions in the soil mass and the BHE components. To tackle this issue, a thorough study has been conducted and it was found that with the use of a proper thermal interaction coefficient at the BHE-soil interface, the temperature distributions in the BHE components and the soil mass become effectively independent of the soil film thickness. In Appendix A, a numerical example highlighting this independency is given.

The spectral analysis is utilized to solve the governing equations on the basis of the fast Fourier transform (FFT). The BHE heat equations are solved using the eigenfunction expansion, and the soil mass heat equation is solved using the modified Bessel function. See Sections 4 and 5.

Step 2: The model in Step 1 is extended to incorporate multiple layers exhibiting different thermal properties using the spectral element method. The spectral element method is an elegant technique combining analytical solutions of a homogeneous domain to the finite element solution of nonhomogeneous domains. Here, the spectral analysis of the BHE-soil domain of Step 1 is discretized into a 2-node spectral element (see Fig. 3). Each soil layer is described by a single spectral element, and a soil mass constituting several layers is described by spectral elements equal in number to the soil layers. The assembly of the spectral element matrices is done similar to the finite element method. See Section 6.

Step 3: The model in Step 2 is extended to incorporate multiple borehole heat exchangers using a superposition technique. The superposition principle is typically applicable to heat sources with Neumann boundary conditions. For Dirichlet boundary conditions, as for the case in this paper, the superposition can only be applied by modifying the temperature amplitude at each heat source by considering the thermal interaction with other heat sources. Using the superposition technique makes the model three-dimensional. See Section 7.

3. Governing equations

Heat equations of a shallow geothermal system consisting of a single U-tube borehole heat exchanger, made of pipe-in, pipe-out, grout, and a soil film, embedded in a soil mass can be described as

Pipe-in

$$\rho c\frac{\partial T_i}{\partial t}dV_i-\lambda\frac{\partial^2 T_i}{\partial z^2}dV_i+\rho cu\frac{\partial T_i}{\partial z}dV_i+b_{ig}(T_i-T_g)dS_{ig}=0 \tag{1}$$

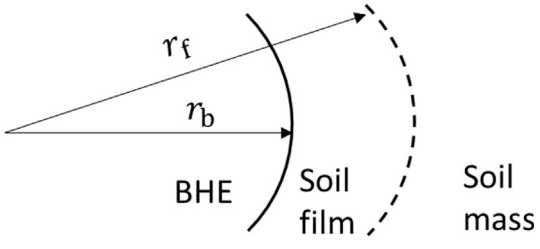

Fig. 2. The boundary between the BHE and the soil film, and the hypothetical boundary between the soil film and the soil mass.

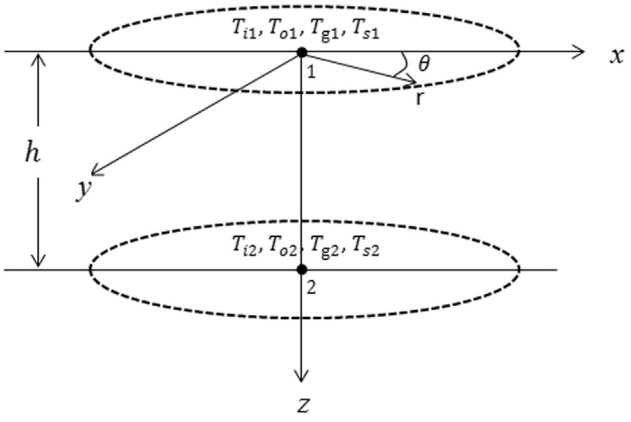

Fig. 3. Two-node spectral element.

Pipe-out

$$\rho c\frac{\partial T_o}{\partial t}dV_o-\lambda\frac{\partial^2 T_o}{\partial z^2}dV_o-\rho cu\frac{\partial T_o}{\partial z}dV_o+b_{og}(T_o-T_g)dS_{og}=0 \tag{2}$$

Grout

$$\rho_g c_g\frac{\partial T_g}{\partial t}dV_g-\lambda_g\frac{\partial^2 T_g}{\partial z^2}dV_g+b_{ig}(T_g-T_i)dS_{ig}+b_{og}(T_g-T_o)dS_{og}+b_{gs}(T_g-T_s)dS_{gs}=0 \tag{3}$$

Soil film

$$\rho_s c_s\frac{\partial T_s}{\partial t}dV_s-\lambda_s\frac{\partial^2 T_s}{\partial z^2}dV_s+b_{gs}(T_s-T_g)dS_{gs}+b_{ss}(T_s-T_{\text{soil}}|_{r=r_f})dS_s=0 \tag{4}$$

Soil mass

$$\frac{1}{\alpha}\frac{\partial T_{\text{soil}}}{\partial t}-\frac{\partial^2 T_{\text{soil}}}{\partial r^2}-\frac{1}{r}\frac{\partial T_{\text{soil}}}{\partial r}=0 \tag{5}$$

where the subscripts i, o, g and s represent pipe-in, pipe-out, grout and soil film, respectively; and $T_i=T_i(z), T_o=T_o(z), T_g=T_g(z), T_s=T_s(z)$ and $T_{\text{soil}}=T_{\text{soil}}(r)$ are the temperatures in pipe-in, pipe-out, grout, soil film and soil mass, respectively. λ, λ_g and λ_s (W/m K) are the thermal conductivity of the circulating fluid, grout and soil film, respectively; u (m/s) is the circulating fluid velocity; b_{ig}, b_{og}, b_{gs}, b_{ss} (W/m^2 K) are the reciprocal of the thermal resistance between pipe-in-grout, pipe-out-grout, grout-soil film, and soil film-soil mass, respectively (see Appendix B for their determination); ρc (J/m^3 K) is the volume heat capacity, with c (J/kg K) the specific heat capacity and ρ (kg/m^3) the mass density; dV_i, dV_o, dV_g, dV_s (m^3) are the control volumes of pipe-in, pipe-out, grout and soil film, respectively; dS_{ig}, dS_{og}, dS_{gs}, dS_s (m^2) are the surface areas of the control volumes of pipe-in, pipe-out, grout and soil film, respectively; r_f is the soil film radius, describing the location of a hypothetical boundary between the soil film and the soil mass (see Fig. 2); and α (m^2/s) is the thermal diffusivity of the soil, described as

$$\alpha=\frac{\lambda_s}{\rho_s c_s} \tag{6}$$

Eq. (4) is a nonhomogeneous partial differential equation due to the presence of $T_{\text{soil}}|_{r=r_f}$. As it will be shown later, this equation will be converted to a homogeneous equation by relating T_{soil} to T_s.

The initial condition is

$$T_i(z,0)=T_o(z,0)=T_g(z,0)=T_s(z,0)=T_{\text{soil}}(r,0) \tag{7}$$

where initially the temperature distribution in the BHE components is equal to that of the steady state condition of the soil mass before the heating/cooling operation starts.

The boundary conditions in the BHE are

$$T_i(0,t) = T_{\text{in}}(t) \tag{8}$$

$$T_i(L,t) = T_o(L,t) \tag{9}$$

where T_{in} is the fluid temperature at $z = 0$, coming from the heat pump. It can have any arbitrary shape in time. Eq. (9) implies that at the bottom of the BHE, $z = L$, the temperature of the fluid in pipe-in is equal to the temperature of the fluid in pipe-out.

The boundary conditions in the soil mass are

$$T_{\text{soil}}|_{r=r_b} = T_s \tag{10}$$

$$T_{\text{soil}}(r=\infty,t) = 0 \tag{11}$$

where Eq. (10) indicates that the soil mass physically includes the soil film and its temperature is equal to the soil film temperature at the boundary with the borehole ($r = r_b$). However, as the soil film has a thickness, the soil mass is hypothetically in contact with the soil film at $r = r_f$, as shown in Fig. 2, and mathematically indicated in Eq. (4). In what follows it will be shown how these two boundaries will be utilized for the determination of the integration constants. Eq. (11) implies that the temperature variation in the soil mass at an infinitely far distance is zero.

4. Solution of soil heat equation

Fourier transform of Eq. (5) gives

$$k_s^2 \hat{T}_{\text{soil}} - \frac{\partial^2 \hat{T}_{\text{soil}}}{\partial r^2} - \frac{1}{r}\frac{\partial \hat{T}_{\text{soil}}}{\partial r} = 0 \tag{12}$$

in which $\hat{T}$ represents the temperature in the frequency domain, and

$$k_s = \sqrt{\frac{i\omega}{\alpha}} \tag{13}$$

is the eigenvalue of the soil mass.

Assume $S = k_s r$, from which the following identities can be derived:

$$\begin{aligned} &\frac{\partial S}{\partial r} = k_s; \quad \left(\frac{\partial S}{\partial r}\right)^2 = k_s^2 \\ &\frac{\partial T}{dS} = \frac{\partial T}{\partial r}\frac{\partial r}{\partial S} = \frac{1}{k_s}\frac{\partial T}{\partial r} \\ &\frac{\partial^2 T}{\partial S^2} = \frac{\partial^2 T}{\partial r^2}\frac{\partial r^2}{\partial S^2} = \frac{1}{k_s^2}\frac{\partial^2 T}{\partial r^2} \end{aligned} \tag{14}$$

Substituting these identities into Eq. (12) gives

$$\hat{T}_{\text{soil}} - \frac{\partial^2 \hat{T}_{\text{soil}}}{\partial S^2} - \frac{1}{S}\frac{\partial \hat{T}_{\text{soil}}}{\partial S} = 0 \tag{15}$$

This equation is a standard modified Bessel function with a general solution expressed as

$$\hat{T}_{\text{soil}}(r) = AI_o(k_s r) + BK_o(k_s r) \tag{16}$$

where I_o and K_o are the modified Bessel functions of the first and second kind.

Applying the boundary condition in Eq. (11) to Eq. (16) leads to

$$\hat{T}_{\text{soil}}\Big|_{r=\infty} = AI_o(\infty) + BK_o(\infty) = 0 \tag{17}$$

but since $I_o(\infty) = \infty$, A in Eq. (17) must be 0, giving:

$$\hat{T}_{\text{soil}}(r) = BK_o(k_s r) \tag{18}$$

At $r = r_b$, Eq. (18) becomes

$$\hat{T}_{\text{soil}}\Big|_{r=r_b} = BK_o(k_s r_b) \tag{19}$$

Applying the boundary condition in Eq. (10) to Eq. (19) yields

$$B = \frac{\hat{T}_s}{K_o(k_s r_b)} \tag{20}$$

Substituting Eq. (20) into Eq. (18), the soil temperature at any radial point can be calculated as

$$\hat{T}_{\text{soil}}(r) = \frac{\hat{T}_s}{K_o(k_s r_b)} K_o(k_s r) \tag{21}$$

At the hypothetical boundary between the soil film and the soil mass, $r = r_f$, Eq. (21) gives

$$\hat{T}_{\text{soil}}\Big|_{r=r_f} = \frac{K_o(k_s r_f)}{K_o(k_s r_b)}\hat{T}_s \tag{22}$$

or, equivalently

$$\hat{T}_{\text{soil}}\Big|_{r=r_f} = A_f \hat{T}_s \tag{23}$$

with

$$A_f = \frac{K_o(k_s r_f)}{K_o(k_s r_b)} \tag{24}$$

which can be substituted into the transformed form of Eq. (4).

5. Solution of BHE heat equations

Applying Fourier transform to Eqs. (1)–(4), and substituting Eq. (23) into the transformed form of Eq. (4), gives

$$-\lambda \frac{\partial^2 \hat{T}_i}{\partial z^2} dV_i + \rho c u \frac{\partial \hat{T}_i}{\partial z} dV_i + (i\omega \rho c dV_i + b_{ig} dS_{ig})\hat{T}_i - b_{ig}\hat{T}_g dS_{ig} = 0 \tag{25}$$

$$-\lambda \frac{\partial^2 \hat{T}_o}{\partial z^2} dV_i - \rho c u \frac{\partial \hat{T}_i}{\partial z} dV_o + (i\omega \rho c dV_o + b_{og} dS_{og})\hat{T}_o - b_{og}\hat{T}_g dS_{og} = 0 \tag{26}$$

$$\begin{aligned} &-\lambda_g \frac{\partial^2 \hat{T}_g}{\partial z^2} dV_g + (i\omega \rho_g c_g dV_g + b_{ig} dS_{ig} + b_{og} dS_{og} + b_{gs} dS_{gs})\hat{T}_g \\ &- b_{ig} dS_{ig}\hat{T}_i - b_{og} dS_{og}\hat{T}_o - b_{gs} dS_{gs}\hat{T}_s = 0 \end{aligned} \tag{27}$$

$$\begin{aligned} &-\lambda_s \frac{\partial^2 \hat{T}_s}{\partial z^2} dV_s + (i\omega \rho_s c_s dV_s + b_{gs} dS_{gs} + b_{ss} dS_s (1 - A_f))\hat{T}_s \\ &- b_{gs} dS_{gs}\hat{T}_g = 0 \end{aligned} \tag{28}$$

which forms a set of homogeneous equations that can be solved using the eigenfunction expansion. This set of homogeneous equations was obtained by converting Eq. (4) from a nonhomogeneous differential equation, due to the presence of the $T_{\text{soil}}|_{r=r_f}$ to a homogeneous equation by incorporating Eq. (23) into Eq. (28).

The solutions to Eqs. (25)–(28) can be expressed as [6]

$$\hat{T}_i = A_i e^{-ikz}, \hat{T}_o = A_o e^{-ikz}, \hat{T}_g = A_g e^{-ikz}, \hat{T}_s = A_s e^{-ikz} \tag{29}$$

in which A_i, A_o, A_g and A_s are the integral constants, and k denotes the system eigenvalues, which need to be determined.

Substituting the solutions in Eq. (29) into Eqs. (25)–(28), following some lengthy but straightforward mathematical derivations (see Appendix C), an eight degree polynomial is obtained of the form:

$$a_0 + a_1 k + a_2 k^2 + a_3 k^3 + a_4 k^4 + a_5 k^5 + a_6 k^6 + a_7 k^7 + a_8 k^8 = 0 \tag{30}$$

This polynomial represents the eigenfunction of a single U-tube BHE, with k denoting its set of eigenvalues determined by solving for the roots of Eq. (30). Only for this set of eigenvalues do the eigenfunction exist and satisfy the boundary conditions of the problem. Eight eigenvalues in two groups of four conjugates are obtained from Eq. (30). The first group is related to the positive heat flow, and the second to the negative heat flow. The exact form of the coefficients of Eq. (30) are given by BniLam and Al-Khoury [4], noting that the term $\sum \bar{A}_m$ should be exchanged by A_f. Though, the exact form of the coefficients can be obtained easily using MAPLE software [10].

6. Modelling multilayer system: The spectral element formulation

The spectral element method is utilized to extend the model from a single borehole heat exchanger embedded in a homogenous soil layer to a multilayer system constituting layers with different physical parameters.

The spectral element method is utilized to formulate an axial symmetric spectral element for heat flow in a coupled borehole heat exchanger and a soil mass. The element consists of two nodes located at its boundaries, and denoting two parallel circular planes within which the heat is constrained to flow, Fig. 3. In the vertical direction, the element extends to cover the whole layer depth, h, and in the radial direction, the element is assumed to extend to infinity.

Consider a one-dimensional heat flow in an element of length h bounded by two nodes: node 1 and node 2. At each node, there are four degrees of freedom, representing the temperatures in pipe-in, pipe-out, grout and soil film. Using Eq. (29) and the eight eigenvalues obtained from solving Eq. (30), the temperatures at any point along the element can be calculated by the superposition of an incident flux from node 1 and a reflective flux from node 2, as

$$\hat{T}_i = A_{i1}e^{-ik_1 z} + B_{i1}e^{-ik_2 z} + C_{i1}e^{-ik_3 z} + D_{i1}e^{-ik_4 z} + A_{i2}e^{-ik_5(h-z)} + B_{i2}e^{-ik_6(h-z)} + C_{i2}e^{-ik_7(h-z)} + D_{i2}e^{-ik_8(h-z)} \tag{31}$$

$$\hat{T}_o = A_{o1}e^{-ik_1 z} + B_{o1}e^{-ik_2 z} + C_{o1}e^{-ik_3 z} + D_{o1}e^{-ik_4 z} + A_{o2}e^{-ik_5(h-z)} + B_{o2}e^{-ik_6(h-z)} + C_{o2}e^{-ik_7(h-z)} + D_{o2}e^{-ik_8(h-z)} \tag{32}$$

$$\hat{T}_g = A_{g1}e^{-ik_1 z} + B_{g1}e^{-ik_2 z} + C_{g1}e^{-ik_3 z} + D_{g1}e^{-ik_4 z} + A_{g2}e^{-ik_5(h-z)} + B_{g2}e^{-ik_6(h-z)} + C_{g2}e^{-ik_7(h-z)} + D_{g2}e^{-ik_8(h-z)} \tag{33}$$

$$\hat{T}_s = A_{s1}e^{-ik_1 z} + B_{s1}e^{-ik_2 z} + C_{s1}e^{-ik_3 z} + D_{s1}e^{-ik_4 z} + A_{s2}e^{-ik_5(h-z)} + B_{s2}e^{-ik_6(h-z)} + C_{s2}e^{-ik_7(h-z)} + D_{s2}e^{-ik_8(h-z)} \tag{34}$$

As for the finite element method, the governing equations are solved in terms of the nodal values. In Appendix D, a complete derivation for the spectral element is given. The derivation leads to a spectral element equation of the form

$$\mathbf{K}(k,\omega_n)\hat{\mathbf{T}}_{\text{node}} = \hat{\mathbf{q}}_{\text{node}} \tag{35}$$

in which $\mathbf{K}(k,\omega_n)$ represents the spectral element matrix, in resemblance to that of the finite element stiffness matrix. However, the spectral element matrix is exact and frequency-dependent. For multiple layers, spectral elements equal in number to the number of layers are assembled in a way similar to that in the finite element method, see Section D.1 in Appendix D.

Upon solving the nodal values, the temperature anywhere within the element can be determined by the inverse fast Fourier transform, as

$$\mathbf{T}(z,t) = \sum_n \begin{pmatrix} \mathbf{A}_1 e^{-ik_1 z} + \mathbf{B}_1 e^{-ik_2 z} + \mathbf{C}_1 e^{-ik_3 z} + \mathbf{D}_1 e^{-ik_4 z} \\ + \mathbf{A}_2 e^{-ik_5(h-z)} + \mathbf{B}_2 e^{-ik_6(h-z)} + \mathbf{C}_2 e^{-ik_7(h-z)} + \mathbf{D}_2 e^{-ik_8(h-z)} \end{pmatrix} e^{i\omega_n t} \tag{36}$$

where $\mathbf{T}(z,t)$ represents $T_i(z,t)$, $T_o(z,t)$, $T_g(z,t)$ or $T_s(z,t)$ in the time domain. The integration constants in Eq. (36) are determined from Eq. (D9) in Appendix D.

Upon solving the temperatures in the BHE, the temperature in the time domain in the soil mass can be determined using Eq. (21), as

$$T_{\text{soil}}(r,z,t) = \sum_n \hat{T}_s(z,\omega)\frac{K_o(k_s r)}{K_o(k_s r_b)}e^{i\omega_n t} \tag{37}$$

7. Modelling multiple borehole heat exchangers: A superposition technique

A superposition technique for Dirichlet boundary conditions is developed to extend the model from a single BHE embedded in an axial symmetric, multilayer domain to multiple borehole heat exchangers embedded in a three-dimensional domain.

Eq. (21) is the solution of the soil heat equation due to a single BHE. Here, we extend this solution to multiple borehole heat exchangers.

Fig. 4 shows a network of $n \times m$ borehole heat exchangers. The radial distance between BHE_i at (x_i, y_i) and BHE_j at (x_j, y_j) is calculated as

$$d_{ij} = \sqrt{x_{ij}^2 + y_{ij}^2} \tag{38}$$

in which $x_{ij} = |x_i - x_j|$ and $y_{ij} = |y_i - y_j|$.

As Eq. (21) imposes Dirichlet boundary condition at the boundary between the soil mass and the BHE, the superposition principle is not directly applicable. The superposition principle works directly for Neumann boundary conditions, and the temperature anywhere in the domain is calculated simply by the algebraic sum of temperatures aroused by heat fluxes from all heat sources. At steady state, the temperature will reach equilibrium and the heat fluxes cease. For Dirichlet boundary conditions, however, the superposition works on condition that the prescribed temper-

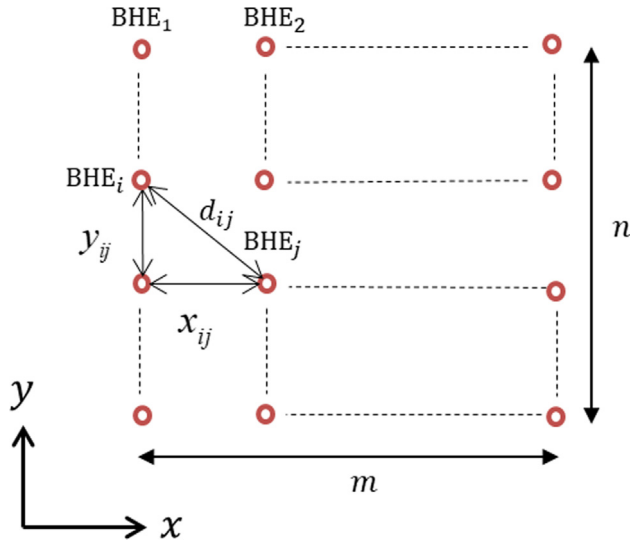

Fig. 4. Multiple borehole heat exchangers configuration.

ature at a borehole must be made equal to the sum of temperatures aroused at its boundary by all boreholes, including itself. This entails modifying the temperature amplitudes at the boreholes and coupling them via a matrix technique, as described hereafter.

The temperature of a soil point at distance r from a BHE can be calculated using Eq. (21), which can be written in a general form as

$$\hat{T}_{\text{soil}}(r) = BK_o(k_s r) \tag{39}$$

For multiple borehole heat exchangers, and following the superposition principle, the temperature of a soil point at distances $r_1 \dots r_N$ from N borehole heat exchangers can be described as

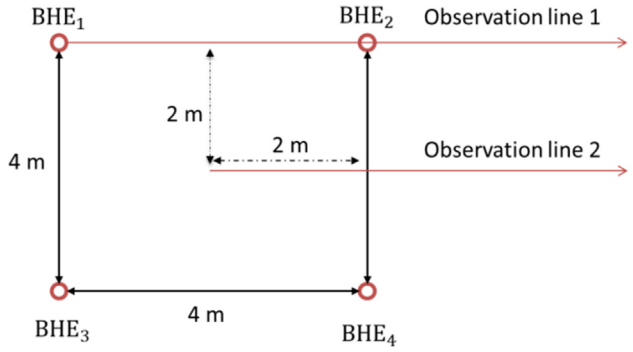

Fig. 5. 4 borehole heat exchangers embedded in a two-layers soil mass.

Table 1
Material and geometrical parameters of the verification example.

Parameter	Value
Borehole:	
Borehole length	10 m
Borehole diameter	0.10 m
U-tube external diameter	0.03 m
U-tube thermal conductivity, λ_p	0.42 W/(m K)
Fluid:	
Density, ρ	1000 kg/m^3
Specific thermal capacity, c	4186 J/(kg K)
Thermal conductivity, λ	0.56 W/(m K)
Dynamic viscosity, μ	0.001 Pa s
Velocity, u	0.1 m/s
Grout:	
Density, ρ_g	1420 kg/m^3
Specific thermal capacity, c_g	1197 J/(kg K)
Thermal conductivity, λ_g	0.65 W/(m K)
Soil:	
Film thickness	2 cm
density, ρ_s	1680 kg/m^3
Specific thermal capacity, c_s	400 J/(kg K)
Thermal conductivity, λ_s at $z \geqslant -5$ m	1 W/(m K)
Thermal conductivity, λ_s at $z \leqslant -5$ m	2 W/(m K)

$$\hat{T}_{\text{soil}}(r) = B_1 K_o(k_s r_1) + B_2 K_o(k_s r_2) + \cdots + B_N K_o(k_s r_N) \tag{40}$$

As mentioned above, the temperature amplitudes $(B_1 \dots B_N)$ at the borehole heat exchangers need to be modified to take into consideration the effect of all involved boreholes. Solving Eq. (40) at the BHE locations, and upon imposing the boundary condition in Eq. (10), it yields

$$\begin{aligned}
\hat{T}_{s1} &= B_1 + B_2 K_o(k_s d_{12}) + \cdots + B_{N-1} K_o(k_s d_{1(N-1)}) + B_N K_o(k_s d_{1N}) \\
\hat{T}_{s2} &= B_1 K_o(k_s d_{21}) + B_2 + \cdots + B_{(N-1)} K_o(k_s d_{2(N-1))}) + B_N K_o(k_s d_{2N}) \\
&\vdots \qquad\qquad \vdots \qquad\qquad \vdots \\
\hat{T}_{sN-1} &= B_1 K_o(k_s d_{(N-1)1}) + B_2 K_o(k_s d_{(N-1)2}) + \cdots + B_{(N-1)} + B_N K_o(k_s d_{(N-1)N}) \\
\hat{T}_{sN} &= B_1 K_o(k_s d_{N1}) + B_2 K_o(k_s d_{N2}) + \cdots + B_{(N-1)} K_o(k_s d_{N(N-1)}) + B_N
\end{aligned} \tag{41}$$

in which d_{12} is the distance between BHE$_1$ and BHE$_2$, etc., as shown in Fig. 4.

In a matrix format, Eq. (41) becomes

$$\begin{pmatrix} \hat{T}_{s1} \\ \hat{T}_{s2} \\ \vdots \\ \hat{T}_{sN-1} \\ \hat{T}_{sN} \end{pmatrix} = \begin{pmatrix} 1 & K_o(k_s d_{12}) & \cdots & K_o(k_s d_{1(N-1)}) & K_o(k_s d_{1N}) \\ K_o(k_s d_{21}) & 1 & \cdots & K_o(k_s d_{2(N-1))}) & K_o(k_s d_{2N}) \\ \vdots & \vdots & \vdots & \vdots & \vdots \\ K_o(k_s d_{(N-1)1}) & K_o(k_s d_{(N-1)2}) & \cdots & 1 & K_o(k_s d_{(N-1)N}) \\ K_o(k_s d_{N1}) & K_o(k_s d_{N2}) & \cdots & K_o(k_s d_{N(N-1)}) & 1 \end{pmatrix} \times \begin{pmatrix} B_1 \\ B_2 \\ \vdots \\ B_{N-1} \\ B_N \end{pmatrix} \tag{42}$$

This equation states that the prescribed temperature at the borehole, $\hat{T}_{s1}$ for instant, is equal to its temperature plus temperatures generated by all other boreholes at its boundary. Its temperature, B_1 in this case, is not its prescribed value, but has to be determined by solving Eq. (42).

Eq. (42) can be expressed as

$$\hat{\mathbf{T}}_s = \mathbf{GB} \tag{43}$$

Solving for **B**, gives

$$\mathbf{B} = \mathbf{G}^{-1}\hat{\mathbf{T}}_s \tag{44}$$

Upon substituting Eq. (44) into Eq. (40), the temperature at any radial point in the soil mass can be calculated.

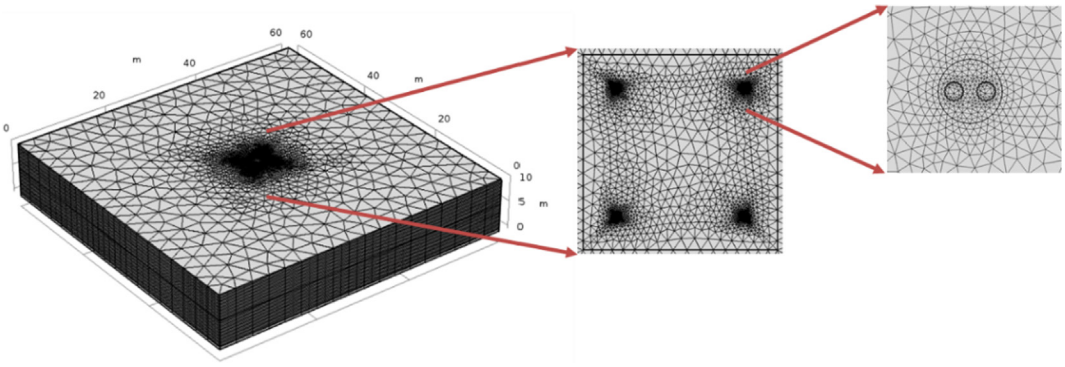

Fig. 6. The finite element mesh.

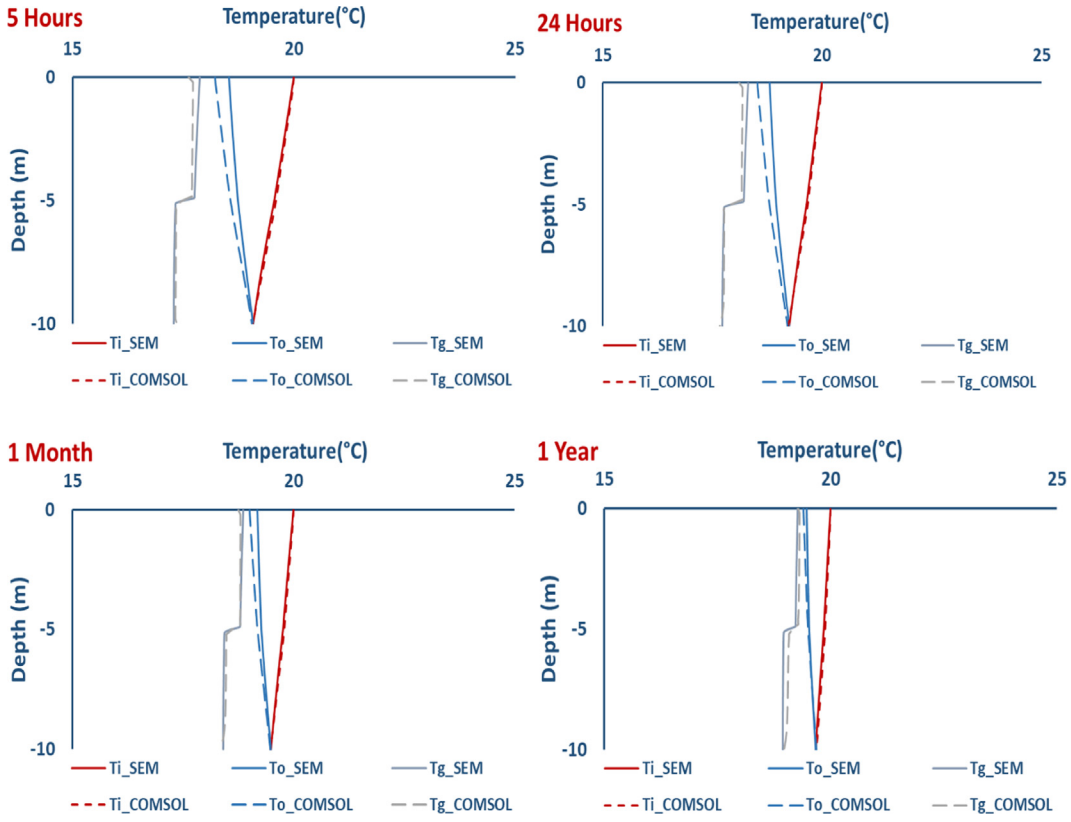

Fig. 7. Temperature profile for pipe-in, pipe-out and grout for one of the 4 BHE's at different times.

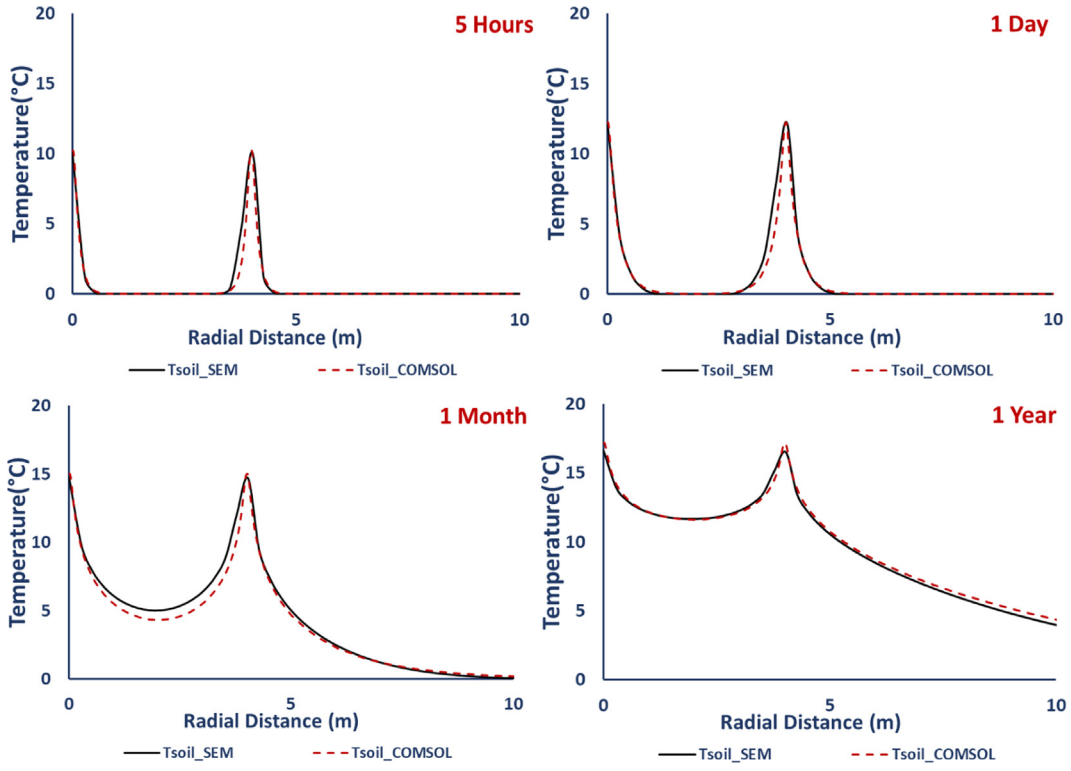

Fig. 8. Radial temperature profile along Observation line1 for the top soil layer.

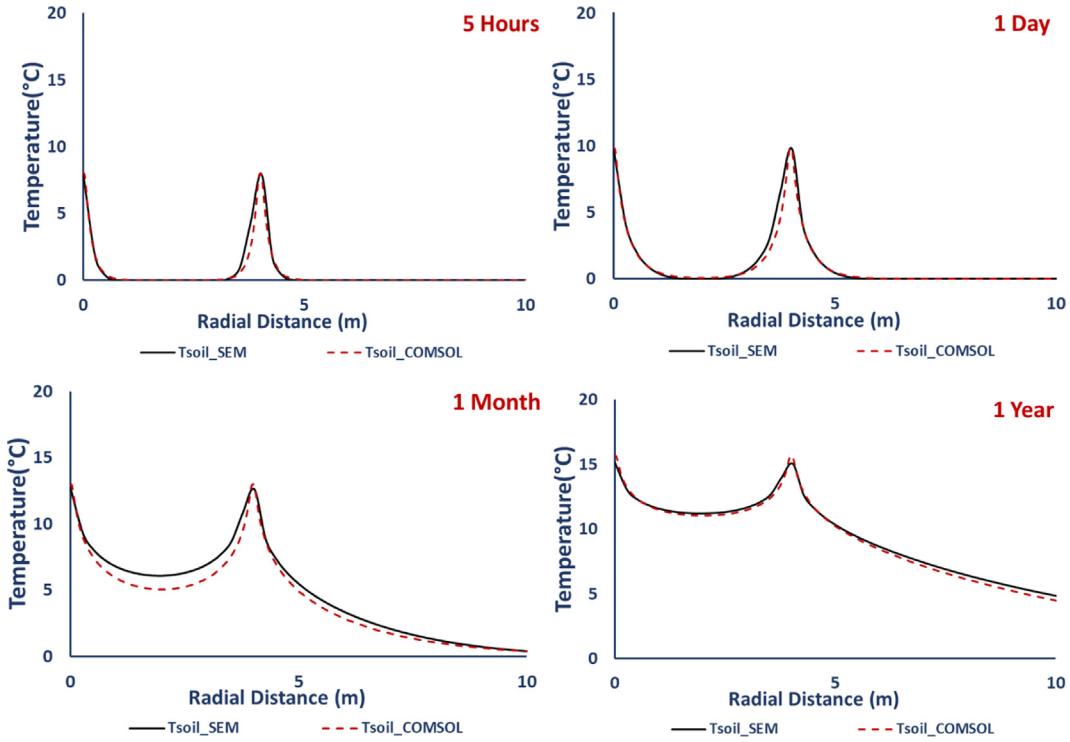

Fig. 9. Radial temperature profile along Observation line 1 for the bottom soil layer.

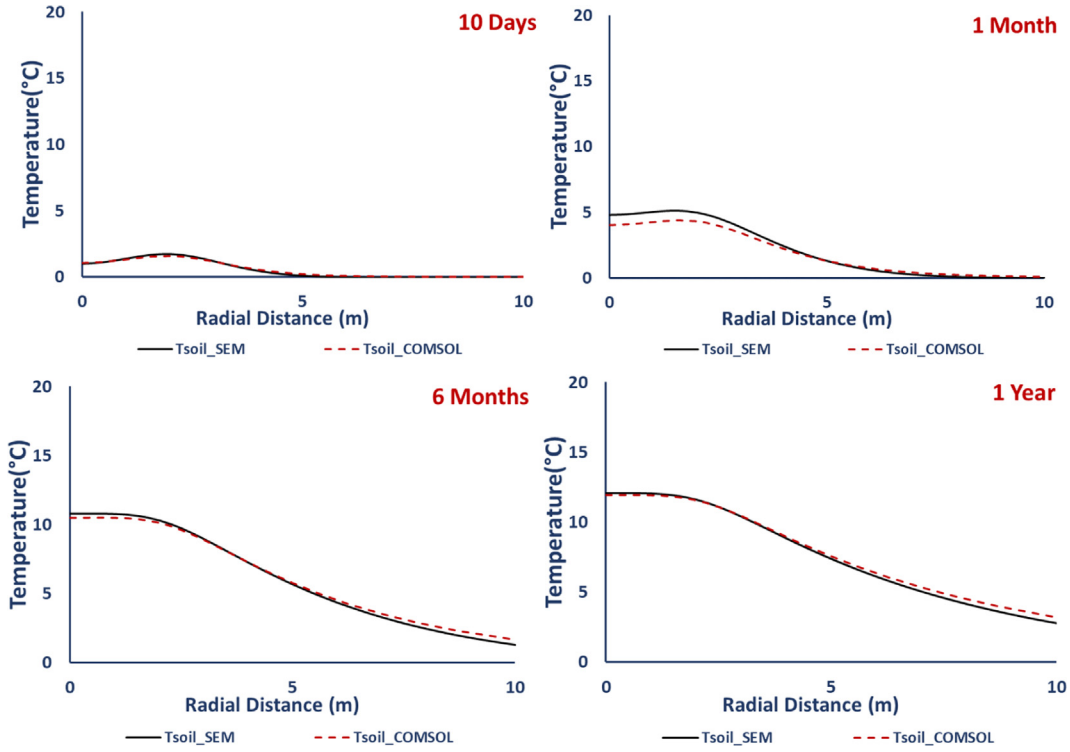

Fig. 10. Radial temperature profile along Observation line 2 for the top soil layer.

8. Model verification

Analytical solution describing heat flow in multiple borehole heat exchangers embedded in a multilayer soil mass has not been introduced before. Accordingly, verification of the proposed model is done by comparing its computational results with those obtained from a detailed finite element model. The finite element package COMSOL Multiphysics (COMSOL 5.2 [5]) is utilized. To reduce the CPU time of the finite element analysis, a relatively small geometry has been designed for this purpose.

A shallow geothermal system constituting four borehole heat exchangers embedded in a soil mass consisting of two soil layers

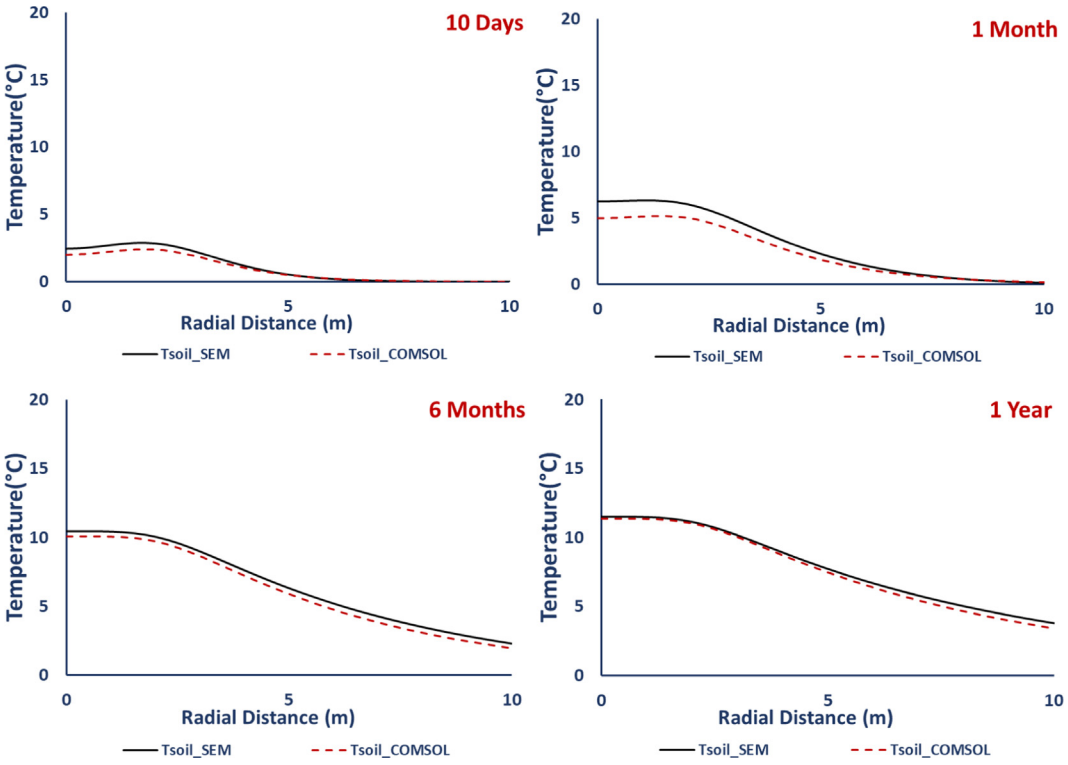

Fig. 11. Radial temperature profile along Observation line 2 for the bottom soil layer.

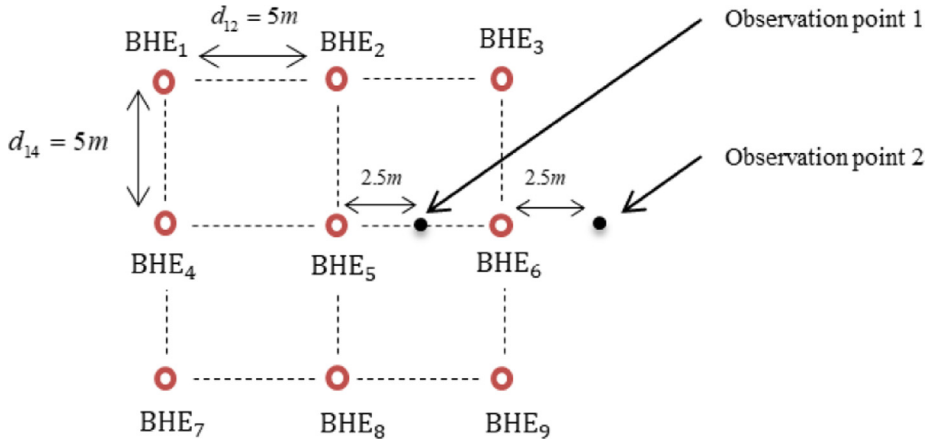

Fig. 12. Borehole heat exchangers configuration.

with different thermal conductivity is modelled. The borehole heat exchangers are assumed 10 m long, constituting a single U-tube and grout. The soil mass is 10 m in depth and consisting of two layers, each 5 m in depth. It radially extends to infinity.

The borehole heat exchangers are configured as shown in Fig. 5. Details of the material and geometrical parameters are given in Table 1. The initial temperature in all components is assumed 0 °C, and the temperature at the inlets of pipe-in (T_{in}) of the four borehole heat exchangers is prescribed to 20 °C.

The spectral element mesh consists of two, 2-node spectral elements. The use of two spectral elements is necessary because the geometry involves two soil layers with different physical parameters. The number of the borehole heat exchangers does not influence the required number of spectral elements, as they are simulated by the superposition technique introduced in Section 7.

The finite element mesh, on the other hand, is made 60 m × 60 m × 10 m, and it consists of 494012, 3D tetrahedral elements, where along the BHE and in the surrounding soil mass, the mesh is made relatively fine. Fig. 6 shows the finite element mesh and the top view at the boreholes region.

Fig. 7 shows the temperature distributions in pipe-in, pipe-out and grout of one of the boreholes as obtained from the spectral element model and the finite element model, for short and long terms of operation. The figure shows a good match between the two results, though a deviation of less than 0.5 °C exists around the outlet of pipe-out. This deviation can be explained as a combination between the inaccuracy of the spectral element model due to the negligence of the radial dimension of the grout, and the typical inaccuracy of the finite element model due to the mesh size effect. Nevertheless, this deviation is relatively small and diminishes as time evolves.

Table 2
Material and geometrical parameters of the numerical example.

Parameter	Value	Parameter	Value
Borehole:		Soil:	
Borehole length	100 m	Film thickness	0.02 m
Borehole diameter	0.1 m	Density, ρ_s	1680 kg/m^3
Pipe external diameter	0.03 m	Specific thermal capacity, c_s	400 J/(kg K)
Pipe thermal conductivity	0.42 W/(m K)		
Fluid:		$0 \geqslant z \geqslant -20$ m	
Density, ρ	1000 kg/m^3	Thermal conductivity, λ_s	2.5 W/(m K)
Specific thermal capacity, c	4186 J/(kg K)	$-20 \geqslant z \geqslant -40$ m	
Thermal conductivity, λ	0.56 W/(m K)	Thermal conductivity, λ_s	1 W/(m K)
Dynamic viscosity, μ	0.001 Pa s	$-40 \geqslant z \geqslant -60$ m	
Velocity, u	0.5 m/s	Thermal conductivity, λ_s	4 W/(m K)
Grout:		$-60 \geqslant z \geqslant -80$ m	
Density, ρ_g	1420 kg/m^3	Thermal conductivity, λ_s	0.5 W/(m K)
Specific thermal capacity, c_g	0.62 W/(m K)	$-80 \geqslant z \geqslant -100$ m	
Thermal conductivity, λ_g	1197 J/(kg K)	Thermal conductivity, λ_s	3 W/(m K)

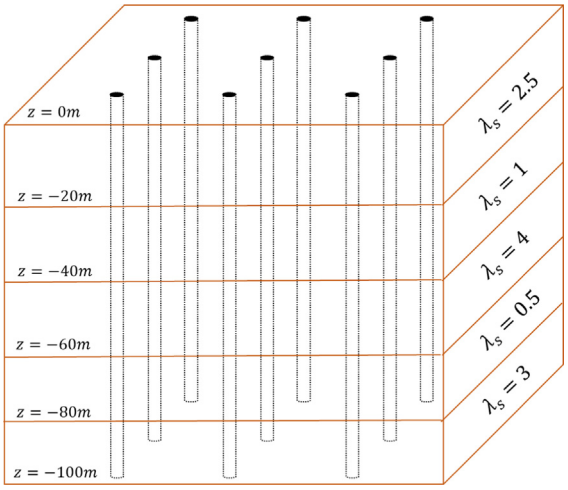

Fig. 13. A schematic representation of the geometry of the numerical example.

Physically, the figure shows a jump at the boundary between the upper and the lower soil layers due to the difference in their thermal conductivities. This demonstrates the capabilities of both computational techniques for simulating such a phenomenon.

Figs. 8 and 9 show the radial soil temperature profile along Observation line 1 (see Fig. 5), for the upper and lower soil layers, respectively. Similarly, Figs. 10 and 11 show the radial soil temperature profile along Observation line 2. The figures show a good match between the two computational results. The small deviation between the results can be attributed to the finite element mesh size, which is relatively coarse in the radial direction. Nevertheless, this deviation is relatively small and diminishes as time evolves.

Physically, the figures show that the temperature profile along Observation line 1 exhibits a clear jump at BHE_1 and BHE_2 locations. This is not apparent along Observation line 2 because it is relatively far from the boreholes. Both models capture this behavior properly.

9. Numerical examples

To demonstrate the model computational capabilities in simulating complicated geometries, a numerical example illustrating heat flow in a 3D shallow geothermal system is studied. The geothermal system is assumed to consist of 9, 100 m in length, borehole heat exchangers embedded in 5 soil layers with highly contrasted thermal properties. The soil thickness is 20 m for each.

A 3 × 3 BHE configuration as shown in Fig. 12 is assumed. The material and geometrical parameters of the geothermal system are given in Table 2 and Fig. 13. The initial temperature in all components is assumed 10 °C, and the temperature at the inlets of pipe-in of the 9 borehole heat exchangers is prescribed to 30 °C. The geometry is simulated using 5, 2-node spectral elements.

The proposed model allows the calculation of temperature distributions in all borehole heat exchangers without differentiation between inner, side and corner boreholes. Here, we present the computational results at the central BHE (BHE_5) and two soil points, indicated as observation points in Fig. 12.

Fig. 14 shows the temperature distributions in pipe-in, pipe-out and grout of BHE_5 on short and long terms of operation. The first figure shows that after 100 s, the fluid has travelled 50 m in pipe-in, giving rise to thermal interaction with the soil via the grout. As a result, the fluid in pipe-in cools down while the grout temperature rises up. Additionally, this figure shows an interesting increase in temperature in pipe-out despite the fact that the fluid hasn't reached it yet. This increase in temperature is due to heat conduction occurring as a result of its direct contact with the grout. At latter times, Fig. 14 shows the effect of the layers thermal conductivities on the temperature distribution in the grout and its influence on pipe-in and pipe-out.

Fig. 15 shows the vertical temperature profile in the soil mass at Observation Points 1 and 2, for short and long terms. The figure shows clearly the jumps in temperatures at the boundaries between layers. The figure also shows an interesting flip in the direction of the temperature jumps at longer terms. In the short term, layers with relatively higher thermal conductivities exhibit faster heat flow, as manifested by the advancing temperature fronts in layers 1, 3 and 5 (see 100 h and 50 days profiles). In the long term, layers with lower thermal conductivities exhibit advancing temperature fronts (see 50 months and 10 years profiles for layers 2 and 4). The reason for this flip is that layers with relatively high thermal conductivities exhibit, at the beginning, faster heat flow, but, later on, faster thermal dissipation. In the contrary, layers with relatively low thermal conductivities exhibit slower heat flow at the beginning and slower thermal dissipation later on. This phenomenon has also been captured and discussed by [1].

Capturing these physical phenomena exhibits clearly the capability of the model to describe the complex nature of heat flow in multiple borehole heat exchangers embedded in multilayer systems.

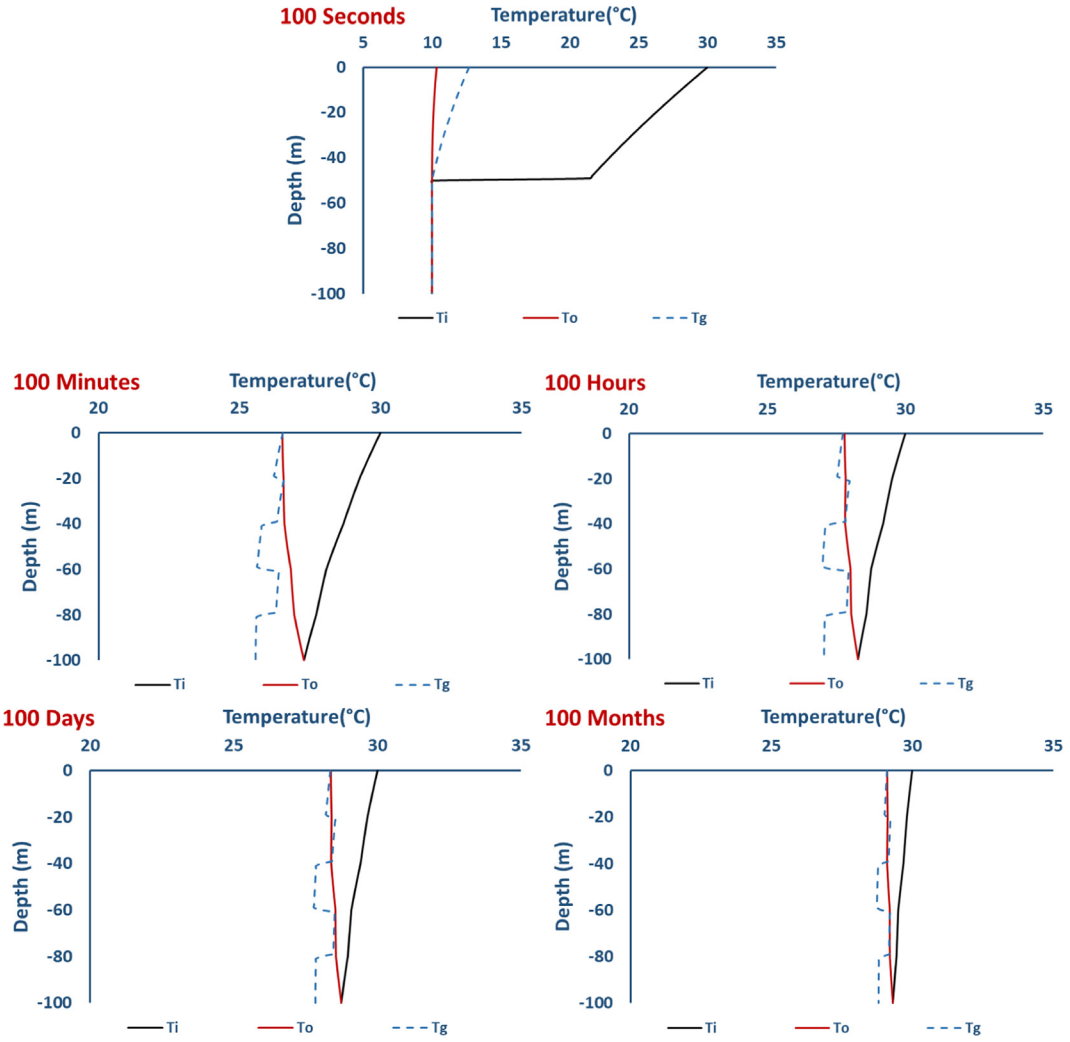

Fig. 14. Temperature in pipe-in, pipe-out and grout for BHE_5 at different times.

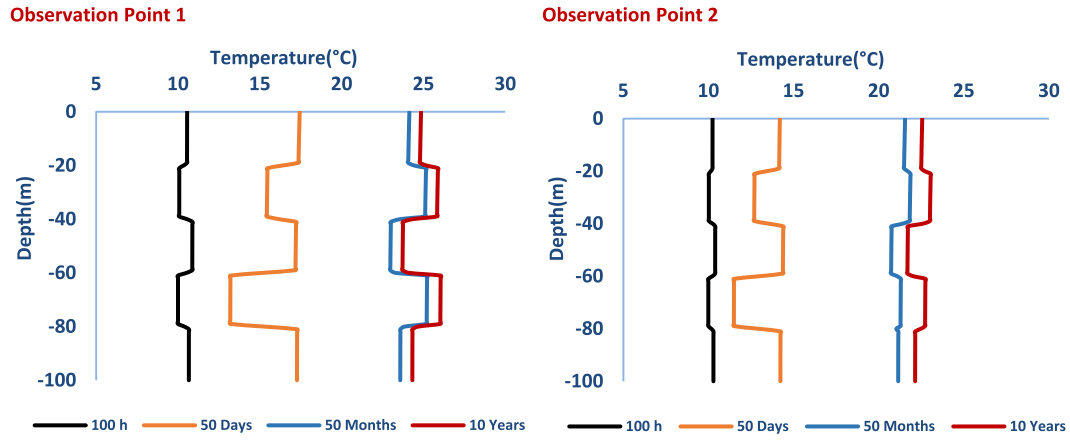

Fig. 15. Vertical soil temperature profiles at different times at observation points 1 and 2.

10. Conclusions

In this paper, a spectral element model for the simulation of transient conduction-convection heat flow in a three-dimensional shallow geothermal system consisting of multiple borehole heat exchangers embedded in a multilayer soil mass is introduced. The model shares the exactness and computational efficiency of the analytical models, and a great extent of generality in describing the geometry and initial and boundary conditions of the numerical techniques. It can describe heat flow is any number of borehole heat exchangers with any layout configuration, embedded in any number of soil layers using minimal CPU time and capacity.

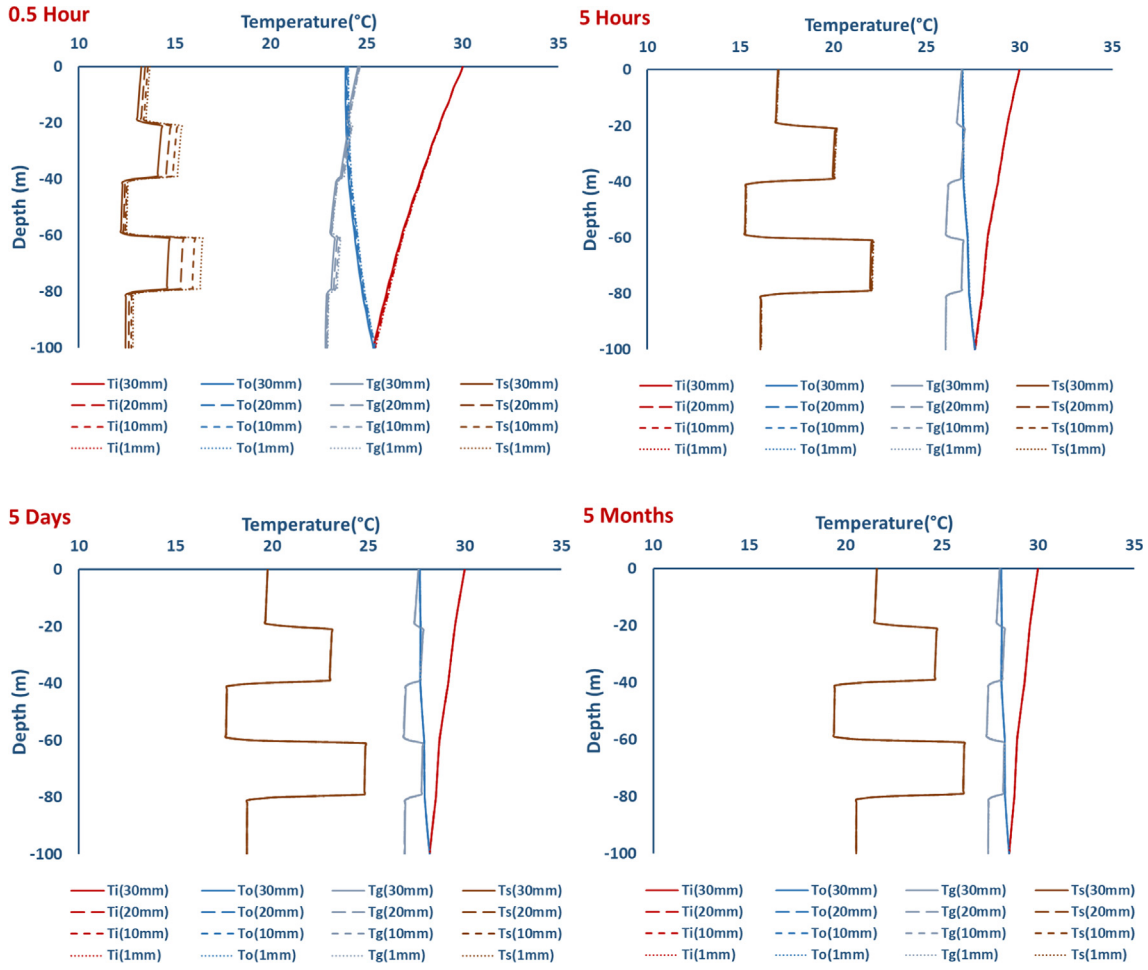

Fig. A1. Pipe-in, pipe-out, grout and soil film temperature distributions using different soil film thicknesses at different times.

The key for obtaining such an exact, computationally efficient and practically general model is the innovative mix between the conceptual model, the mathematical model and the solution technique. The link between 1D domain (for the borehole), axial symmetric 2D domain (for a homogeneous soil layer) and 3D domain (for multiple layers), together with the use of the soil film, makes the conceptual model mathematically feasible. Changing the BHE-soil non-homogeneous differential equations to homogenous differential equations (see Eqs. (4) and (23)) together with the matrix formulation for coupling the boreholes (see Eq. (40)), makes the mathematical model solvable. The use of the spectral element method for modelling multilayer systems together with the superposition technique for modelling multiple borehole heat exchangers makes the solution technique fit to the physics of the problem and computationally efficient.

Appendix A. Soil-film thickness

In this appendix, we highlight the independence of the temperature distributions in the BHE components and the soil mass on the soil film thickness.

To minimize the effect of the soil film thickness on the temperature distributions, the thermal interaction coefficients must be appropriately formulated. In pursuit of this, the thermal interaction coefficients given in Appendix B are proved to be the most appropriate. Using these coefficients, we here demonstrate the model-independency on the soil film via a numerical example. The geometry and material properties, together with the initial and boundary conditions, are as for the numerical example given in Section 9.

Fig. A1 shows the temperature distributions in pipe-in, pipe-out, grout and soil film for a single BHE at 0.5 h, 5 h, 5 days and 5 months, using 1 mm, 10 mm, 20 mm and 30 mm soil film thicknesses. The figure clearly shows that the soil film thickness has practically no effect on the temperature distributions except at 0.5 h where there is a deviation of around 1–2 °C between 1 mm and 30 mm, mainly in the lower thermal conductivity layers.

Fig. A2 shows the corresponding temperature distributions in the soil mass in the third layer. Obviously, the temperature distribution in the soil mass has not been affected by the soil film thickness, except at 0.5 h where there is little deviation between 1 mm and 30 mm soil film thicknesses.

Appendix B. Thermal interaction coefficients

The thermal interaction coefficient for pipe-in - grout is described as

$$b_{ig} = \frac{1}{R_i} \tag{B1}$$

where

$$R_i = R_{\text{convection}} + R_{\text{pipe material}} = \frac{1}{r_o/r_i h} + \frac{r_o \ln(r_o/r_i)}{\lambda_p} \tag{B2}$$

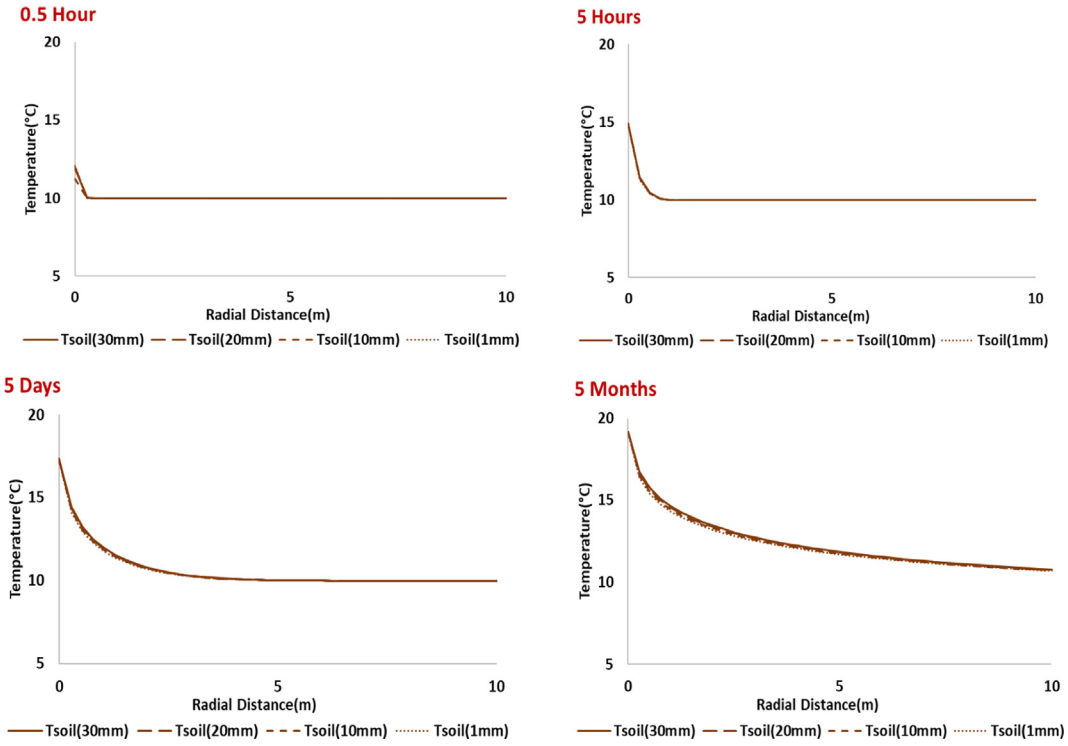

Fig. A2. Soil radial temperature distribution in the third layer using different soil film thickness at different times.

in which r_i and r_o are the inner and outer radius of pipe-in, respectively; λ_p is the thermal conductivity of pipe-in material; and $\bar{h} = Nu\lambda/D$ is the convective heat transfer coefficient, where D is the inner diameter of the pipe, Nu and λ are the Nusselt Number and the thermal conductivity of the circulating fluid. A similar formulation is valid for pipe-out-grout, b_{og}.

The thermal interaction coefficient for grout –soil film can be expressed as

$$b_{gs} = \frac{1}{R_g} \tag{B3}$$

where

$$R_g = \frac{r_b \ln(r_b/r_{eq})}{\lambda_g} \tag{B4}$$

in which r_b is the radius of the grout (borehole), and $r_{eq} = \sqrt{r_{in}^2 + r_{out}^2}$ with r_{in} the pipe-in inner radius and r_{out} the pipe-out inner radius.

The thermal interaction coefficient for the soil film-soil mass can be expressed as

$$b_{ss} = \frac{1}{R_s} \tag{B5}$$

where

$$R_s = \frac{r_f \ln(r_f/r_b)}{\lambda_s} \tag{B6}$$

in which r_f is the radius of the soil film.

Appendix C. Eigenvalue determination

Substituting Eq. (29) into Eqs. (25)–(28), gives

$$k^2\lambda dV_i A_i e^{-ikz} - ik\rho cudV_i A_i e^{-ikz} + (i\omega\rho cdV_i + b_{ig}dS_{ig})A_i e^{-ikz} - b_{ig}dS_{ig}A_g e^{-ikz} = 0 \tag{C1}$$

$$k^2\lambda dV_i A_o e^{-ikz} + ik\rho cudV_o A_i e^{-ikz} + (i\omega\rho cdV_o + b_{og}dS_{og})A_o e^{-ikz} - b_{og}dS_{og}A_g e^{-ikz} = 0 \tag{C2}$$

$$k^2\lambda_g dV_g A_g e^{-ikz} + (i\omega\rho_g c_g dV_g + b_{ig}dS_{ig} + b_{og}dS_{og} + b_{gs}dS_{gs})A_g e^{-ikz} - b_{ig}dS_{ig}A_i e^{-ikz} - b_{og}dS_{og}A_o e^{-ikz} - b_{gs}dS_{gs}A_s e^{-ikz} = 0 \tag{C3}$$

$$k^2\lambda_s dV_s A_s e^{-ikz} + (i\omega\rho_s c_s dV_s + b_{gs}dS_{gs} + b_{ss}dS_s(1-A_f))A_s e^{-ikz} - b_{gs}dS_{gs}A_g e^{-ikz} = 0 \tag{C4}$$

Dividing Eqs. (C1)–(C4) by e^{-ikz}, rearranging and putting it in a matrix form, gives

$$\begin{pmatrix} a_{11} & 0 & a_{13} & 0 \\ 0 & a_{22} & a_{23} & 0 \\ a_{31} & a_{32} & a_{33} & a_{34} \\ 0 & 0 & a_{43} & a_{44} \end{pmatrix} \begin{bmatrix} A_i \\ A_o \\ A_g \\ A_s \end{bmatrix} = 0 \tag{C5}$$

where

$$a_{11} = k^2\lambda dV_i - ik\rho cudV_i + i\omega\rho cdV_i + b_{ig}dS_{ig}$$
$$a_{13} = -b_{ig}dS_{ig}$$
$$a_{22} = k^2\lambda dV_o + ik\rho cudV_o + i\omega\rho cdV_o + b_{og}dS_{og}$$
$$a_{23} = -b_{og}dS_{og}$$
$$a_{31} = -b_{ig}dS_{ig}$$
$$a_{32} = -b_{og}dS_{og}$$
$$a_{33} = k^2\lambda_g dV_g + i\omega\rho_g c_g dV_g + b_{ig}dS_{ig} + b_{og}dS_{og} + b_{gs}dS_{gs}$$
$$a_{34} = -b_{gs}dS_{gs}$$
$$a_{43} = -b_{gs}dS_{gs}$$
$$a_{44} = k^2\lambda_s dV_s + i\omega\rho_s c_s dV_s + b_{gs}dS_{gs} + b_{ss}dS_s(1-A_f)$$

Since $\hat{T}_i$, $\hat{T}_g$, $\hat{T}_o$ and $\hat{T}_s$ are coupled, the constants, A_i, A_o, A_g and A_s are related to each other. Using Eqs. (C1)–(C5), the following relationships exist:

Pipe-in-grout

$$A_i = Y^{ig} A_g$$
$$Y^{ig} = \frac{b_{ig} dS_{ig}}{k^2 \lambda dV_i \mp ik\rho cudV_i + i\omega\rho cdV_i + b_{ig} dS_{ig}} \tag{C6}$$

Pipe-out-grout

$$A_o = Y^{og} A_g$$
$$Y^{og} = \frac{b_{og} dS_{og}}{k^2 \lambda dV_o \pm ik\rho cudV_o + i\omega\rho cdV_o + b_{og} dS_{og}} \tag{C7}$$

Soil film-grout

$$A_s = Y^{sg} A_g$$
$$Y^{sg} = \frac{b_{gs} dS_{gs}}{k^2 \lambda_s dV_s + i\omega\rho_s c_s dV_s + b_{gs} dS_{gs} + b_{ss} dS_s (1 - A_f)} \tag{C8}$$

For each k there is a corresponding Y^{ig}, Y^{og} and Y^{sg}, i.e. there are Y_1^{ig}, Y_1^{og}, Y_1^{sg} for k_1, etc. [7].

The $\mp$ signs in Eqs. (C6) and (C7) refer to the fluid velocity direction at the nod. The fluid velocity in pipe-in at nod 1 is (−), while it is (+) at nod 2 (see Fig. 2). For pipe-out, the signs are opposite.

Non-trivial solution of Eq. (C5) can only be obtained by letting the determinate equal to zero, giving a complex eight degree polynomial of the form:

$$a_8 k^8 + a_7 k^7 + a_6 k^6 + a_5 k^5 + a_4 k^4 + a_3 k^3 + a_2 k^2 + a_1 k + a_0 = 0 \tag{C9}$$

Appendix D. Spectral element formulation, assembly and solution

Consider a one-dimensional heat flow in an element of length h bounded by two nodes: node 1 and node 2, Fig. 2. At each node, there are four degrees of freedom, representing the temperatures in pipe-in, pipe-out, grout and soil film. Using Eq. (29), the temperatures at any point along the element are calculated by the superposition of an incident flux, from node 1, and a reflective flux, from node 2, as

$$\hat{T}_i = A_{i1} e^{-ik_1 z} + B_{i1} e^{-ik_2 z} + C_{i1} e^{-ik_3 z} + D_{i1} e^{-ik_4 z} + A_{i2} e^{-ik_5 (h-z)} + B_{i2} e^{-ik_6 (h-z)} + C_{i2} e^{-ik_7 (h-z)} + D_{i2} e^{-ik_8 (h-z)} \tag{D1}$$

$$\hat{T}_o = A_{o1} e^{-ik_1 z} + B_{o1} e^{-ik_2 z} + C_{o1} e^{-ik_3 z} + D_{o1} e^{-ik_4 z} + A_{o2} e^{-ik_5 (h-z)} + B_{o2} e^{-ik_6 (h-z)} + C_{o2} e^{-ik_7 (h-z)} + D_{o2} e^{-ik_8 (h-z)} \tag{D2}$$

$$\hat{T}_g = A_{g1} e^{-ik_1 z} + B_{g1} e^{-ik_2 z} + C_{g1} e^{-ik_3 z} + D_{g1} e^{-ik_4 z} + A_{g2} e^{-ik_5 (h-z)} + B_{g2} e^{-ik_6 (h-z)} + C_{g2} e^{-ik_7 (h-z)} + D_{g2} e^{-ik_8 (h-z)} \tag{D3}$$

$$\hat{T}_s = A_{s1} e^{-ik_1 z} + B_{s1} e^{-ik_2 z} + C_{s1} e^{-ik_3 z} + D_{s1} e^{-ik_4 z} + A_{s2} e^{-ik_5 (h-z)} + B_{s2} e^{-ik_6 (h-z)} + C_{s2} e^{-ik_7 (h-z)} + D_{s2} e^{-ik_8 (h-z)} \tag{D4}$$

As for the finite element method, the governing equations are solved in terms of the nodal values.

At node 1, z = 0, substituting Eqs. (C6)–(C8) into Eqs. (D1), (D2) and (D4), the nodal temperatures become

$$\begin{aligned}
\hat{T}_{i1} &= A_{g1} Y_1^{ig} + B_{g1} Y_2^{ig} + C_{g1} Y_3^{ig} + D_{g1} Y_4^{ig} + A_{g2} Y_5^{ig} e^{-ik_5 h} + B_{g2} Y_6^{ig} e^{-ik_6 h} + C_{g2} Y_7^{ig} e^{-ik_7 h} + D_{g2} Y_8^{ig} e^{-ik_8 h} \\
\hat{T}_{o1} &= A_{g1} Y_1^{og} + B_{g1} Y_2^{og} + C_{g1} Y_3^{og} + D_{g1} Y_4^{og} + A_{g2} Y_5^{og} e^{-ik_5 h} + B_{g2} Y_6^{og} e^{-ik_6 h} + C_{g2} Y_7^{og} e^{-ik_7 h} + D_{g2} Y_8^{og} e^{-ik_8 h} \\
\hat{T}_{g1} &= A_{g1} + B_{g1} + C_{g1} + D_{g1} + A_{g2} e^{-ik_5 h} + B_{g2} e^{-ik_6 h} + C_{g2} e^{-ik_7 h} + D_{g2} e^{-ik_8 h} \\
\hat{T}_{s1} &= A_{g1} Y_1^{sg} + B_{g1} Y_2^{sg} + C_{g1} Y_3^{sg} + D_{g1} Y_4^{sg} + A_{g2} Y_5^{sg} e^{-ik_5 h} + B_{g2} Y_6^{sg} e^{-ik_6 h} + C_{g2} Y_7^{sg} e^{-ik_7 h} + D_{g2} Y_8^{sg} e^{-ik_8 h}
\end{aligned} \tag{D5}$$

At node 2, z = h, and similarly, upon substituting Eqs. (C6)–(C8) into Eqs. (D1), (D2) and (D4), the nodal temperatures become

$$\begin{aligned}
\hat{T}_{i2} &= A_{g1} Y_1^{ig} e^{-ik_1 h} + B_{g1} Y_2^{ig} e^{-ik_2 h} + C_{g1} Y_3^{ig} e^{-ik_3 h} + D_{g1} Y_4^{ig} e^{-ik_4 h} + A_{g2} Y_5^{ig} + B_{g2} Y_6^{ig} + C_{g2} Y_7^{ig} + D_{g2} Y_8^{ig} \\
\hat{T}_{o2} &= A_{g1} Y_1^{og} e^{-ik_1 h} + B_{g1} Y_2^{og} e^{-ik_2 h} + C_{g1} Y_3^{og} e^{-ik_3 h} + D_{g1} Y_4^{og} e^{-ik_4 h} + A_{g2} Y_5^{og} + B_{g2} Y_6^{og} + C_{g2} Y_7^{og} + D_{g2} Y_8^{og} \\
\hat{T}_{g2} &= A_{g1} e^{-ik_1 h} + B_{g1} e^{-ik_2 h} + C_{g1} e^{-ik_3 h} + D_{g1} e^{-ik_4 h} + A_{g2} + B_{g2} + C_{g2} + D_{g2} \\
\hat{T}_{s2} &= A_{g1} Y_1^{sg} e^{-ik_1 h} + B_{g1} Y_2^{sg} e^{-ik_2 h} + C_{g1} Y_3^{sg} e^{-ik_3 h} + D_{g1} Y_4^{sg} e^{-ik_4 h} + A_{g2} Y_5^{sg} + B_{g2} Y_6^{sg} + C_{g2} Y_7^{sg} + D_{g2} Y_8^{sg}
\end{aligned} \tag{D6}$$

$$\begin{pmatrix} \hat{T}_{i1} \\ \hat{T}_{o1} \\ \hat{T}_{g1} \\ \hat{T}_{s1} \\ \hat{T}_{i2} \\ \hat{T}_{g2} \\ \hat{T}_{o2} \\ \hat{T}_{s2} \end{pmatrix} = \begin{pmatrix} Y_1^{ig} & Y_2^{ig} & Y_3^{ig} & Y_4^{ig} & Y_5^{ig} e^{-ik_5 h} & Y_6^{ig} e^{-ik_6 h} & Y_7^{ig} e^{-ik_7 h} & Y_8^{ig} e^{-ik_8 h} \\ Y_1^{og} & Y_2^{og} & Y_3^{og} & Y_4^{og} & Y_5^{og} e^{-ik_5 h} & Y_6^{og} e^{-ik_6 h} & Y_7^{og} e^{-ik_7 h} & Y_8^{og} e^{-ik_8 h} \\ 1 & 1 & 1 & 1 & e^{-ik_5 h} & e^{-ik_6 h} & e^{-ik_7 h} & e^{-ik_8 h} \\ Y_1^{sg} & Y_2^{sg} & Y_3^{sg} & Y_4^{sg} & Y_5^{sg} e^{-ik_5 h} & Y_6^{sg} e^{-ik_6 h} & Y_7^{sg} e^{-ik_7 h} & Y_8^{sg} e^{-ik_8 h} \\ Y_1^{ig} e^{-ik_1 h} & Y_2^{ig} e^{-ik_2 h} & Y_3^{ig} e^{-ik_3 h} & Y_4^{ig} e^{-ik_4 h} & Y_5^{ig} & Y_6^{ig} & Y_7^{ig} & Y_8^{ig} \\ Y_1^{og} e^{-ik_1 h} & Y_2^{og} e^{-ik_2 h} & Y_3^{og} e^{-ik_3 h} & Y_4^{og} e^{-ik_4 h} & Y_5^{og} & Y_6^{og} & Y_7^{og} & Y_8^{og} \\ e^{-ik_1 h} & e^{-ik_2 h} & e^{-ik_3 h} & e^{-ik_4 h} & 1 & 1 & 1 & 1 \\ Y_1^{sg} e^{-ik_1 h} & Y_2^{sg} {}_2 e^{-ik_2 h} & Y_3^{sg} e^{-ik_3 h} & Y_4^{sg} e^{-ik_4 h} & Y_5^{sg} & Y_6^{sg} & Y_7^{sg} & Y_8^{sg} \end{pmatrix} \begin{pmatrix} A_{g1} \\ B_{g1} \\ C_{g1} \\ D_{g1} \\ A_{g2} \\ B_{g2} \\ C_{g2} \\ D_{g2} \end{pmatrix} \tag{D7}$$

In a matrix form, Eqs. (D5) and (D6) can be presented as which indicates that the temperatures of pipe-in, pipe-out and soil film are represented in terms of the grout coefficients. This equation can be written as

$$\hat{\mathbf{T}}_{\text{node}} = \mathbf{H}(k, \omega_n)\mathbf{A} \tag{D8}$$

Solving for **A**, gives

$$\mathbf{A} = \mathbf{H}(k, \omega_n)^{-1} \hat{\mathbf{T}}_{\text{node}} \tag{D9}$$

The next step is to relate the heat flux to the temperature at the nodes. The heat fluxes for the BHE components are

$$
\begin{aligned}
q_i &= \mp\lambda \frac{\partial T_i}{\partial z} dA_i \\
q_o &= \mp\lambda \frac{\partial T_o}{\partial z} dA_o \\
q_g &= \mp\lambda_g \frac{\partial T_g}{\partial z} dA_g \\
q_s &= \mp\lambda_s \frac{\partial T_s}{\partial z} dA_s
\end{aligned} \tag{D10}
$$

where dA_i, dA_o, dA_g and dA_s are the cross-sectional areas of pipe-in, pip-out, grout and soil film respectively. The $\mp$ sign refers to the direction of the heat flux: the heat flux at node 1 is $(-)$ while at node 2, it is $(+)$.

Substituting Eqs. (C6)–(C8) into Eqs. (D1), (D2) and (D4), gives

$$
q_i = \mp\lambda dA_i \begin{pmatrix} -ik_1 A_{g1} Y_1^{ig} e^{-ik_1 z} - ik_2 B_{g1} Y_2^{ig} e^{-ik_2 z} \\ -ik_3 C_{g1} Y_3^{ig} e^{-ik_3 z} - ik_4 D_{g1} Y_4^{ig} e^{-ik_4 z} \\ +ik_5 A_{g2} Y_5^{ig} e^{-ik_5 (h-z)} + ik_6 B_{g2} Y_6^{ig} e^{-ik_6 (h-z)} \\ +ik_7 C_{g2} Y_7^{ig} e^{-ik_7 (h-z)} + ik_8 D_{g2} Y_8^{ig} e^{-ik_8 (h-z)} \end{pmatrix} \tag{D11}
$$

$$
q_o = \mp\lambda dA_o \begin{pmatrix} -ik_1 A_{g1} Y_1^{og} e^{-ik_1 z} - ik_2 B_{g1} Y_2^{og} e^{-ik_2 z} \\ -ik_3 C_{g1} Y_3^{og} e^{-ik_3 z} - ik_4 D_{g1} Y_4^{og} e^{-ik_4 z} \\ +ik_5 A_{g2} Y_5^{og} e^{-ik_5 (h-z)} + ik_6 B_{g2} Y_6^{og} e^{-ik_6 (h-z)} \\ +ik_7 C_{g2} Y_7^{og} e^{-ik_7 (h-z)} + ik_8 D_{g2} Y_8^{og} e^{-ik_8 (h-z)} \end{pmatrix} \tag{D12}
$$

$$
q_g = \mp\lambda_g dA_g \begin{pmatrix} -ik_1 A_g e^{-ik_1 z} - ik_2 B_g e^{-ik_2 z} \\ -ik_3 C_g e^{-ik_3 z} - ik_4 D_g e^{-ik_4 z} \\ +ik_5 A_{g2} e^{-ik_5 (h-z)} + ik_6 B_{g2} e^{-ik_6 (h-z)} \\ +ik_7 C_{g2} e^{-ik_7 (h-z)} + ik_8 D_{g2} e^{-ik_8 (h-z)} \end{pmatrix} \tag{D13}
$$

$$
q_s = \mp\lambda_s dA_s \begin{pmatrix} -ik_1 A_{g1} Y_1^{sg} e^{-ik_1 z} - ik_2 B_{g1} Y_2^{sg} e^{-ik_2 z} \\ -ik_3 C_{g1} Y_3^{sg} e^{-ik_3 z} - ik_4 D_{g1} Y_4^{sg} e^{-ik_4 z} \\ +ik_5 A_{g2} Y_5^{sg} e^{-ik_5 (h-z)} + ik_6 B_{g2} Y_6^{sg} e^{-ik_6 (h-z)} \\ +ik_7 C_{g2} Y_7^{sg} e^{-ik_7 (h-z)} + ik_8 D_{g2} Y_8^{sg} e^{-ik_8 (h-z)} \end{pmatrix} \tag{D14}
$$

At the element nodes, Eqs. (D11)–(D14) become:

At node 1, z = 0:

$$
q_{i1} = -\lambda dA_i \begin{pmatrix} -ik_1 A_{g1} Y_1^{ig} - ik_2 B_{g1} Y_2^{ig} - ik_3 C_{g1} Y_3^{ig} - ik_4 D_{g1} Y_4^{ig} \\ +ik_5 A_{g2} Y_5^{ig} e^{-ik_5 h} + ik_6 B_{g2} Y_6^{ig} e^{-ik_6 h} + ik_7 C_{g2} Y_7^{ig} e^{-ik_7 h} \\ +ik_8 D_{g2} Y_8^{ig} e^{-ik_8 h} \end{pmatrix}
$$

$$
q_{o1} = -\lambda dA_o \begin{pmatrix} -ik_1 A_{g1} Y_1^{og} - ik_2 B_{g1} Y_2^{og} - ik_3 C_{g1} Y_3^{og} - ik_4 D_{g1} Y_4^{og} \\ +ik_5 A_{g2} Y_5^{og} e^{-ik_5 h} + ik_6 B_{g2} Y_6^{og} e^{-ik_6 h} + ik_7 C_{g2} Y_7^{og} e^{-ik_7 h} \\ +ik_8 D_{g2} Y_8^{og} e^{-ik_8 h} \end{pmatrix}
$$

$$
q_{g1} = -\lambda_g dA_g \begin{pmatrix} -ik_1 A_g - ik_2 B_g - ik_3 C_g - ik_4 D_g \\ +ik_5 A_{g2} e^{-ik_5 h} + ik_6 B_{g2} e^{-ik_6 h} + ik_7 C_{g2} e^{-ik_7 h} \\ +ik_8 D_{g2} e^{-ik_8 h} \end{pmatrix}
$$

$$
q_{s1} = -\lambda_s dA_s \begin{pmatrix} -ik_1 A_{g1} Y_1^{sg} - ik_2 B_{g1} Y_2^{sg} - ik_3 C_{g1} Y_3^{sg} - ik_4 D_{g1} Y_4^{sg} \\ +ik_5 A_{g2} Y_5^{sg} e^{-ik_5 h} + ik_6 B_{g2} Y_6^{sg} e^{-ik_6 h} \\ +ik_7 C_{g2} Y_7^{sg} e^{-ik_7 h} + ik_8 D_{g2} Y_8^{sg} e^{-ik_8 h} \end{pmatrix} \tag{D15}
$$

At node 2, z = h:

$$
q_{i2} = \lambda dA_i \begin{pmatrix} -ik_1 A_{g1} Y_1^{ig} e^{-ik_1 h} - ik_2 B_{g1} Y_2^{ig} e^{-ik_2 h} - ik_3 C_{g1} Y_3^{ig} e^{-ik_3 h} \\ -ik_4 D_{g1} Y_4^{ig} e^{-ik_4 h} \\ +ik_5 A_{g2} Y_5^{ig} + ik_6 B_{g2} Y_6^{ig} + ik_7 C_{g2} Y_7^{ig} + ik_8 D_{g2} Y_8^{ig} \end{pmatrix}
$$

$$
q_{o2} = \lambda dA_o \begin{pmatrix} -ik_1 A_{g1} Y_1^{og} e^{-ik_1 h} - ik_2 B_{g1} Y_2^{og} e^{-ik_2 h} - ik_3 C_{g1} Y_3^{og} e^{-ik_3 h} \\ -ik_4 D_{g1} Y_4^{og} e^{-ik_4 h} \\ +ik_5 A_{g2} Y_5^{og} + ik_6 B_{g2} Y_6^{og} + ik_7 C_{g2} Y_7^{og} + ik_8 D_{g2} Y_8^{og} \end{pmatrix}
$$

$$
q_{g2} = \lambda_g dA_g \begin{pmatrix} -ik_1 A_g e^{-ik_1 h} - ik_2 B_g e^{-ik_2 h} - ik_3 C_g e^{-ik_3 h} - ik_4 D_g e^{-ik_4 h} \\ +ik_5 A_{g2} + ik_6 B_{g2} + ik_7 C_{g2} + ik_8 D_{g2} \end{pmatrix}
$$

$$
q_{s2} = \lambda_s dA_s \begin{pmatrix} -ik_1 A_{g1} Y_1^{sg} e^{-ik_1 h} - ik_2 B_{g1} Y_2^{sg} e^{-ik_2 h} - ik_3 C_{g1} Y_3^{sg} e^{-ik_3 h} \\ -ik_4 D_{g1} Y_4^{sg} e^{-ik_4 h} \\ +ik_5 A_{g2} Y_5^{sg} + ik_6 B_{g2} Y_6^{sg} + ik_7 C_{g2} Y_7^{sg} + ik_8 D_{g2} Y_8^{sg} \end{pmatrix} \tag{D16}
$$

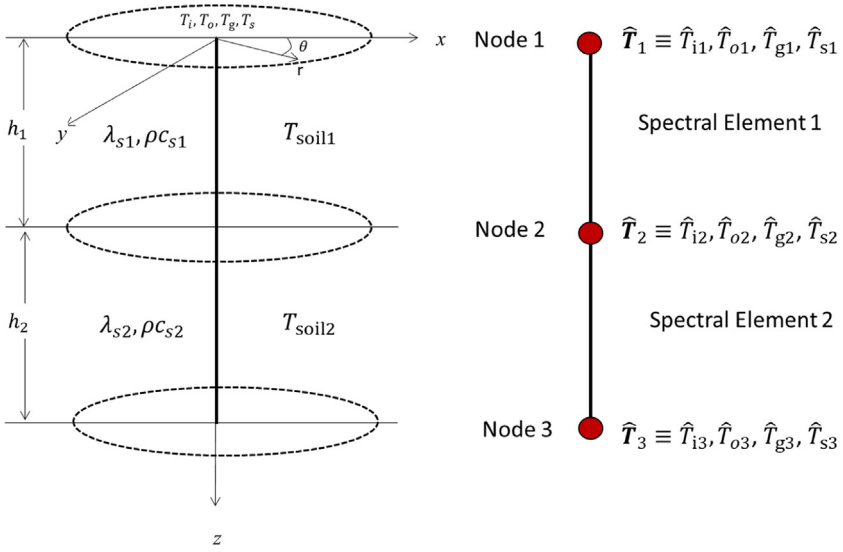

Fig. D1. Two-layer system and its spectral element discretization.

In a matrix form:

$$\begin{pmatrix} q_{i1} \\ q_{o1} \\ q_{g1} \\ q_{s1} \\ q_{i2} \\ q_{o2} \\ q_{g2} \\ q_{s2} \end{pmatrix} = \begin{pmatrix} b_{11} & b_{12} & b_{13} & b_{14} & b_{15} & b_{16} & b_{17} & b_{18} \\ b_{21} & b_{22} & b_{23} & b_{24} & b_{25} & b_{26} & b_{27} & b_{28} \\ b_{31} & b_{32} & b_{33} & b_{34} & b_{35} & b_{36} & b_{37} & b_{38} \\ b_{41} & b_{42} & b_{43} & b_{44} & b_{45} & b_{46} & b_{47} & b_{48} \\ b_{51} & b_{52} & b_{53} & b_{54} & b_{55} & b_{56} & b_{57} & b_{58} \\ b_{61} & b_{62} & b_{63} & b_{64} & b_{65} & b_{66} & b_{67} & b_{68} \\ b_{71} & b_{72} & b_{73} & b_{74} & b_{75} & b_{76} & b_{77} & b_{78} \\ b_{88} & b_{82} & b_{83} & b_{84} & b_{85} & b_{86} & b_{87} & b_{88} \end{pmatrix} \begin{pmatrix} A_{g1} \\ B_{g1} \\ C_{g1} \\ D_{g1} \\ A_{g2} \\ B_{g2} \\ C_{g2} \\ D_{g2} \end{pmatrix} \tag{D17}$$

where

$$\begin{aligned}
b_{11} &= ik_1 Y_1^{ig} \lambda dA_i & b_{21} &= ik_1 Y_1^{og} \lambda dA_o & b_{31} &= ik_1 \lambda_g dA_g & b_{41} &= ik_1 Y_1^{sg} \lambda_s dA_s \\
b_{12} &= ik_2 Y_2^{ig} \lambda dA_i & b_{22} &= ik_2 Y_2^{og} \lambda dA_o & b_{32} &= ik_2 \lambda_g dA_g & b_{42} &= ik_2 Y_2^{sg} \lambda_s dA_s \\
b_{13} &= ik_3 Y_3^{ig} \lambda dA_i & b_{23} &= ik_3 Y_3^{og} \lambda dA_o & b_{33} &= ik_3 \lambda_g dA_g & b_{43} &= ik_3 Y_3^{sg} \lambda_s dA_s \\
b_{14} &= ik_4 Y_4^{ig} \lambda dA_i & b_{24} &= ik_4 Y_4^{og} \lambda dA_o & b_{34} &= ik_4 \lambda_g dA_g & b_{44} &= ik_4 Y_4^{sg} \lambda_s dA_s \\
b_{15} &= -ik_5 Y_5^{ig} \lambda dA_i e^{-ik_5 h} & b_{25} &= -ik_5 Y_5^{og} \lambda dA_o e^{-ik_5 h} & b_{35} &= -ik_5 \lambda_g dA_g e^{-ik_5 h} & b_{45} &= -ik_5 Y_5^{sg} \lambda_s dA_s e^{-ik_5 h} \\
b_{16} &= -ik_6 Y_6^{ig} \lambda dA_i e^{-ik_6 h} & b_{26} &= -ik_6 Y_6^{og} \lambda dA_o e^{-ik_6 h} & b_{36} &= -ik_6 \lambda_g dA_g e^{-ik_6 h} & b_{46} &= -ik_6 Y_6^{sg} \lambda_s dA_s e^{-ik_6 h} \\
b_{17} &= -ik_7 Y_7^{ig} \lambda dA_i e^{-ik_7 h} & b_{27} &= -ik_7 Y_7^{og} \lambda dA_o e^{-ik_7 h} & b_{37} &= -ik_7 \lambda_g dA_g e^{-ik_7 h} & b_{47} &= -ik_7 Y_7^{sg} \lambda_s dA_s e^{-ik_7 h} \\
b_{18} &= -ik_8 Y_8^{ig} \lambda dA_i e^{-ik_8 h} & b_{28} &= -ik_8 Y_8^{og} \lambda dA_o e^{-ik_8 h} & b_{38} &= -ik_8 \lambda_g dA_g e^{-ik_8 h} & b_{48} &= -ik_8 Y_8^{sg} \lambda_s dA_s e^{-ik_8 h} \\
b_{51} &= -ik_1 Y_1^{ig} \lambda dA_i e^{-ik_1 h} & b_{61} &= -ik_1 Y_1^{og} \lambda dA_o e^{-ik_1 h} & b_{71} &= -ik_1 \lambda_g dA_g e^{-ik_1 h} & b_{81} &= -ik_1 Y_1^{sg} \lambda_s dA_s e^{-ik_1 h} \\
b_{52} &= -ik_2 Y_2^{ig} \lambda dA_i e^{-ik_2 h} & b_{62} &= -ik_2 Y_2^{og} \lambda dA_o e^{-ik_2 h} & b_{72} &= -ik_2 \lambda_g dA_g e^{-ik_2 h} & b_{82} &= -ik_2 Y_2^{sg} \lambda_s dA_s e^{-ik_2 h} \\
b_{53} &= -ik_3 Y_3^{ig} \lambda dA_i e^{-ik_3 h} & b_{63} &= -ik_3 Y_3^{og} \lambda dA_o e^{-ik_3 h} & b_{73} &= -ik_3 \lambda_g dA_g e^{-ik_3 h} & b_{83} &= -ik_3 Y_3^{sg} \lambda_s dA_s e^{-ik_3 h} \\
b_{54} &= -ik_4 Y_4^{ig} \lambda dA_i e^{-ik_4 h} & b_{64} &= -ik_4 Y_4^{og} \lambda dA_o e^{-ik_4 h} & b_{74} &= -ik_4 \lambda_g dA_g e^{-ik_4 h} & b_{84} &= -ik_4 Y_4^{sg} \lambda_s dA_s e^{-ik_4 h} \\
b_{55} &= ik_5 Y_5^{ig} \lambda dA_i & b_{65} &= ik_5 Y_5^{og} \lambda dA_o & b_{75} &= ik_5 \lambda_g dA_g & b_{85} &= ik_5 Y_5^{sg} \lambda_s dA_s \\
b_{56} &= ik_6 Y_6^{ig} \lambda dA_i & b_{66} &= ik_6 Y_6^{og} \lambda dA_o & b_{76} &= ik_6 \lambda_g dA_g & b_{86} &= ik_6 Y_6^{sg} \lambda_s dA_s \\
b_{57} &= ik_7 Y_7^{ig} \lambda dA_i & b_{67} &= ik_7 Y_7^{og} \lambda dA_o & b_{77} &= ik_7 \lambda_g dA_g & b_{87} &= ik_7 Y_7^{sg} \lambda_s dA_s \\
b_{58} &= ik_8 Y_8^{ig} \lambda dA_i & b_{68} &= ik_8 Y_8^{og} \lambda dA_o & b_{78} &= ik_8 \lambda_g dA_g & b_{88} &= ik_8 Y_8^{sg} \lambda_s dA_s
\end{aligned}$$

This equation can be described as

$$\hat{\mathbf{q}}_{\text{node}} = \mathbf{M}(k, \omega_n)\mathbf{A} \tag{D18}$$

Substituting Eq. (D9) into Eq. (D18), yields

$$\hat{\mathbf{q}}_{\text{node}} = \mathbf{K}(k, \omega_n)\hat{\mathbf{T}}_{\text{node}} \tag{D19}$$

in which $\mathbf{K}(k, \omega_n) = \mathbf{M}(k, \omega_n)\mathbf{H}(k, \omega_n)^{-1}$, representing the spectral element stiffness matrix, in resemblance to that of the finite element method. However, the spectral element matrix is exact and frequency-dependent.

D.1. Global matrix assembly and solution

For a multilayer system, each layer is described by a spectral element. The assembly of the global matrix is done following the finite element method, in which matrices assembly is dictated by the elements and nodes numbers. In this assembly process, the way the nodes are numbered determines the locations of the coefficients in the global stiffness matrix.

Consider a borehole heat exchanger embedded in a two layer system shown schematically in Fig. D1. The system is described by two spectral elements and three nodes, numbered as shown in the figure. Each node has four degrees of freedom, describing the temperatures in pipe-in, $\hat{T}_i$, pipe-out, $\hat{T}_o$, grout, $\hat{T}_g$, and soil film, $\hat{T}_s$. The stiffness matrix for each element is described by Eq. (D19). Using the finite element method, the global spectral element equation can then be described as

$$\begin{bmatrix} K_{11}^1 & K_{12}^1 & \\ K_{21}^1 & K_{22}^1 + K_{11}^2 & K_{12}^2 \\ & K_{21}^2 & K_{22}^2 \end{bmatrix} \begin{Bmatrix} \hat{\mathbf{T}}_1 \\ \hat{\mathbf{T}}_2 \\ \hat{\mathbf{T}}_3 \end{Bmatrix} = \begin{Bmatrix} \hat{\mathbf{q}}_1 \\ \hat{\mathbf{q}}_2 \\ \hat{\mathbf{q}}_3 \end{Bmatrix} \tag{D20}$$

in which the matrix on the left-hand side of the equation is the global stiffness matrix, with the superscript indices indicating the layer (element) number. The vector on the left-hand side is the degrees of freedom vector, indicating the nodal temperatures that need to be determined; and the vector on the right-hand side is the force vector, indicating the corresponding nodal heat fluxes.

The solution of the global system of equations is conducted using the IMSL mathematical library subroutine, *lin_sol_gen*, which solves a general system of linear equations $Ax = b$, (IMSL [13]). Eq. (C9) is solved using the IMSL subroutine, *DZPOCC*, which solves for the roots of a polynomial with complex coefficients. The reconstruction of the time domain is carried out using the inverse FFT algorithm.

References

[1] S.L. Abdelaziz, T.Y. Ozudogru, C.G. Olgun, J.R. Martin, Multilayer finite line source model for vertical heat exchangers, Geothermics 51 (2014) 406–416.

[2] R. Al-Khoury, Computational Modeling of Shallow Geothermal Systems, CRC Press/Taylor & Francis Group, 2012.

[3] N. BniLam, R. Al-Khoury, Transient heat conduction in an infinite medium subjected to multiple cylindrical heat sources: An application to shallow geothermal systems, Renew. Energy 97 (2016) 145–154.

[4] N. BniLam, R. Al-Khoury, A spectral element model for nonhomogeneous heat flow in shallow geothermal systems, Int. J. Heat Mass Transf. 104 (2017) 703–717.

[5] COMSOL 5.2, Multiphysics Modeling, http://www.comsol.com/comsol-multiphysics (Accessed April 2017).

[6] J.F. Doyle, Wave Propagation in Structures: Spectral Analysis Using Fast Discrete Fourier Transforms, Springer-Verlag, New York, 1997.

[7] J.F. Doyle, Spectral analysis of coupled thermoelastic waves, J. Therm. Stresses 11 (1988) 175–185.

[8] Erol Selçuk, Hashemi Mir Amid, François Bertrand, Analytical solution of discontinuous heat extraction for sustainability and recovery aspects of borehole heat exchangers, Int. J. Therm. Sci. 88 (2015) 47–58.
[9] P. Eskilson, J. Claesson, Simulation model for thermally interacting heat extraction boreholes, Numer. Heat Transfer 13 (1988) 149–165.
[10] Maple, mathematical software. Available at http://www.maplesoft.com/products/maple/ (Accessed July 2017).
[11] P. Pasquier, D. Marcotte, Efficient computation of heat flux signals to ensure the reproduction of prescribed temperatures at several interacting heat sources, Appl. Therm. Eng. 59 (2013) 515–526.
[12] J. Raymond, L. Lamarche, Simulation of thermal response tests in a layered subsurface, Appl. Energy 109 (2013) 293–301.
[13] IMSL Numerical Libraries http://www.roguewave.com/products-services/imsl-numerical-libraries (Last accessed 2018).